

Charged-current neutrino opacity within the relativistic Hartree-Fock framework for astrophysical simulations of core-collapse supernovae and binary neutron star mergers

Kamil Sokolowski^{1,2,*}, Anil Kumar^{1,†} and Tobias Fischer^{1,3,‡}

¹*Institute of Theoretical Physics, Wrocław University of Science and Technology,
Wybrzeże Wyspiańskiego 27, 50-370 Wrocław, Poland*

²*Institute of Theoretical Physics, University of Wrocław, plac Maxa Borna 9, 50-204 Wrocław, Poland*

³*Research Center for Computational Physics and Data Processing,
Institute of Physics, Silesian University in Opava,
Bezručovo nám. 13, CZ-746-01 Opava, Czech Republic*

(Dated: May 19, 2026)

Neutrinos and their weak interactions play a vital role in the physics of core-collapse supernovae and binary neutron star mergers. Their description within astrophysical simulations, including the weak rates, is of pivotal importance not only for the prediction of accurate neutrino fluxes and spectra, including the associated conditions relevant to nucleosynthesis, neutrinos are also responsible for heating and cooling of the stellar plasma as well as the transport of lepton number and entropy. In the present article, we develop an essential improvement of the description of the underlying nuclear medium, necessary for the calculations of charged-current weak rates, with the inclusion of explicitly momentum-dependent nuclear interactions. To this end, we introduce the relativistic Hartree-Fock (RHF) approach and the associated momentum-dependent nucleon self-energies. We discuss the resulting neutrino and antineutrino opacities and find large discrepancies comparing the weak rates at the RHF level with those of commonly used relativistic mean-field (RMF) models; in particular, we observe a substantial shift of previously reported large medium-dependent modifications associated with the RMF approach.

I. INTRODUCTION

Neutrinos are abundantly produced in astrophysical environments where high temperatures are encountered, on the order of several tens of MeV, such as core-collapse supernovae and binary neutron star mergers. They are not only confirmed messengers of the central engine that drives massive star explosions— $\bar{\nu}_e$ were detected from the last nearby event SN1987A by the four operating water Cherenkov neutrino detectors through the inverse β -decay [1–5]—neutrinos also contribute to the associated shock revival through heating and cooling processes via a variety of weak reactions. More details on the role of core-collapse supernova phenomenology can be found in Ref. [6]. Furthermore, neutrinos play a crucial role in the nucleosynthesis of both core-collapse supernovae and binary neutron star mergers [7], in particular for the late-time ejection, during which the proton-to-baryon ratio, which is given by the electron fraction Y_e , is determined by the flux and spectral differences between ν_e and $\bar{\nu}_e$. Neutrinos are also subject to oscillations due to their small but finite rest masses, a phenomenon that necessitates the kinetic approach, unlike the commonly employed transport methods in astrophysical simulations (cf. Ref. [8] and references therein).

It is therefore of paramount interest to provide accurate neutrino flux and spectra predictions from simulations of core-collapse supernovae and binary neutron star

mergers. This, in turn, requires the consistent treatment of weak processes, in particular those involving a nuclear component and the nuclear medium, which has been realized in one of the pioneering works providing first-principle expressions for weak rates [9]. Charged-current weak rates, treating nucleons at the mean-field level, were later applied to self-consistent simulations of massive star explosions [10, 11]. These models were based on general relativistic neutrino radiation hydrodynamics in spherical symmetry, featuring three-flavor Boltzmann neutrino transport [12, 13]. The simulations covered the long-term evolution of the deleptonizing proto-neutron star, i.e. the central compact remnant of a supernova explosion, which deleptonizes and later cools via the emission of neutrinos of all flavors. These models provide the first reliable predictions of the nucleosynthesis associated with massive star explosions, including the neutrino-driven wind, initially exhibiting only a minor neutron excess, making them incompatible with the rapid neutron-capture process and later evolving toward proton-rich conditions. Later continuous updates of these models confirm the initial findings [14, 15]. It is important to note that these findings based on spherically symmetric models are insufficient and need to be explored in a multi-dimensional setup; e.g., it has been demonstrated that proto-neutron star convection has a dominating impact on deleptonization [6, 16–18].

The present paper extends these previous developments by treating the nuclear medium beyond the mean-field approach. Therefore, a nuclear equation of state (EOS) is developed based on the relativistic Hartree-Fock (RHF) approach [19]. The essential difference, with relevance to the weak rates, is the presence of momentum-

* kamil.sokolowski@pwr.edu.pl

† anil.1@iitj.ac.in

‡ bert-tobias.fischer@pwr.edu.pl

dependent interactions, expressed in terms of the nucleon self-energies. These, in turn, change the neutrino-energy dependence of the charged-current weak rates in comparison to the commonly employed relativistic mean-field (RMF) approach [9], i.e. Hartree mean-field approximation and, furthermore, alter the density-dependence of these rates.

The paper is organized as follows. In Sec. II, we will revisit the weak interaction physics for the charged-current weak rates, followed in Sec. III with the novel RHF expressions. In Sec. IV, we provide a detailed evaluation of the neutrino absorption rates at selected conditions encountered in core-collapse supernovae and binary neutron star mergers. In Sec. V, we perform a comparison between neutrino rates within RHF approach and the RMF model, which was obtained via the proper reduction of the RHF model. Special emphasis is given to the comparison with the mean-field treatment, for which the essential expressions are provided in Appendix B. The manuscript closes with a summary and concluding remarks in Sec. VI. In this paper, we use the following notation $k_B = \hbar = c = 1$ and $g^{\mu\nu} = \text{diag}(+1, -1, -1, -1)$.

II. CHARGED-CURRENT NEUTRINO OPACITY

In the following, we focus on the class of charged-current weak processes:

$$\nu_1(p_1) + N_2(p_2) \longrightarrow l_3(p_3) + N_4(p_4) , \quad (1)$$

determined by the exchange of W^\pm bosons (wavy lines in Fig. 1), for neutrinos (+) and antineutrinos (-), and where $l_3 \equiv l$ denotes the leptons (e, μ, τ), particle 1 is the corresponding lepton neutrino, $\nu_i \equiv \nu_l$ and N_i ($i = 2, 4$) correspond to the initial and final state baryons.

In order to calculate the neutrino absorption rate for process (1) at finite temperature and density, we apply the real-time formalism and the Kobes-Semenoff rules [20, 21], which state that at the lowest order in the weak coupling constant and to all orders in the strong coupling constant [20], the interaction (absorption) rate can be obtained from

$$\Gamma(E_1) = \frac{1}{2E_1} \text{Tr} \left\{ \not{p}_1 \Sigma_1^>(E_1, \mathbf{p}_1) \right\} , \quad (2)$$

where $m_1 \approx 0$, the slash denotes the Feynman notation, $\not{p} = \gamma^\mu p_\mu$ and \mathbf{p} denotes the 3-momentum. The neutrino self-energy, $\Sigma_1^>$, presented by Fig. 1, is obtained by applying the cutting rules at finite temperature following Ref. [21]:

$$\begin{aligned} \Sigma_1^>(E_1, \mathbf{p}_1) &= \frac{G_F^2 C^2}{2} \int \frac{d^4 p_2}{(2\pi)^4} \int \frac{d^4 p_3}{(2\pi)^4} \bar{V}_\mu^1 G_3^>(p_3) V_\nu^1 \\ &\times \left[-\text{Tr} \left\{ G_2^<(p_2) \bar{V}_h^\mu G_4^>(p_4) V_h^\nu \right\} \right] , \quad (3) \end{aligned}$$

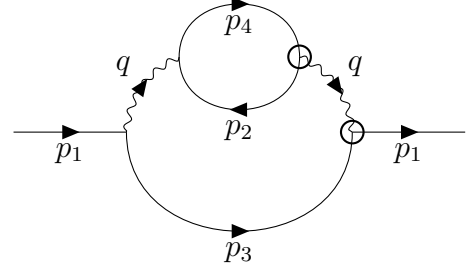


FIG. 1. Diagrammatic form of the neutrino self-energy, $\Sigma_1^>(E_1, \mathbf{p}_1)$, for process (1), which is used for the cutting rules at finite temperature. Solid lines are the fermions and the wavy lines are the exchanged vector bosons W^+ (for neutrinos) and W^- (for antineutrinos), with *standard* uncircled and circled vertices. We note here that we have the inserted boson self-energy presented by the one-loop with particles 2 and 4 and that cutting the diagram in half results in the usual Feynman diagram for process (1) at the tree level for the resulting left-hand side.

where V_μ and $\bar{V}_\mu = \gamma^0 V_\mu^\dagger \gamma^0$ are the hadron (h) and lepton (l) vertex functions. The Dirac propagators in the real-time formalism are given by

$$G_a^>(p_a) = 2\pi (\not{p}_a + m_a) [1 - f_a(p_a^0)] \Theta(p_a^0) \delta(p_a^2 - m_a^2) , \quad (4)$$

$$G_a^<(p_a) = -2\pi (\not{p}_a + m_a) f_a(p_a^0) \Theta(p_a^0) \delta(p_a^2 - m_a^2) , \quad (5)$$

where " $>$ " and " $<$ " denote flow into and out of the circled vertex, respectively, $f_a(p_a^0) = [1 + \exp\{(p_a^0 - \mu_a)/T\}]^{-1}$ is the Fermi-Dirac distribution function for particle species a with the corresponding chemical potential, μ_a , Θ denotes the Heaviside step function, and $p_a^\mu = (p_a^0, \mathbf{p})$ is the 4-momentum ($a = 1, 2, 3, 4$). We note here that when dealing with antiparticles, we have the following replacement, $\not{p}_a + m_a \longrightarrow \not{p}_a - m_a$ in Eqs. (4) and (5).

Furthermore, Eq. (3) is obtained for the current-current interaction described by the following Lagrangian [9]

$$\mathcal{L} = \frac{G_F C}{\sqrt{2}} l^\mu j_\mu^{cc} , \quad (6)$$

where $C = \cos\theta_C$ (we take $\sin\theta_C = 0.053$ for the processes considered in this paper) is the cosine of the Cabibbo up-down quark mixing angle with no exchange of strangeness, for which we have the following leptonic vertex, $V_\mu^1 = \gamma_\mu (1 - \gamma_5)$, giving rise to the leptonic current, $l^\mu = \bar{\psi}_3 V_1^\mu \psi_1$, and the hadronic vertex,

$$V_h^\mu = \gamma^\mu (g_V - \gamma_5 g_A) + F_2 \frac{i\sigma^{\mu\alpha} q_\alpha}{2M_N} - \frac{G_P}{M_N} \gamma_5 q^\mu , \quad (7)$$

defining the hadronic current, $j_\mu^{cc} = \bar{\psi}_4 V_\mu^h \psi_2$, where ψ_a and $\bar{\psi}_a$ are the Dirac spinors for the initial- and final state fermions.

The 4-momentum transfer is denoted as $q^\mu = (q_0, \mathbf{q})$ for which we have $q^\mu = p_1^\mu - p_3^\mu = p_4^\mu - p_2^\mu$ and $q_\mu^2 = q_0^2 - \mathbf{q}^2$, with $q \equiv |\mathbf{q}|$, and $\sigma^{\mu\nu} = \frac{i}{2}[\gamma^\mu, \gamma^\nu]$. Note further that $M_N = (m_n + m_p)/2$ is the average nucleon mass with bare neutron and proton rest masses, m_n and m_p , respectively. The different contributions to the hadronic current (7) can then be expressed as follows,

$$\text{LO : } \quad g_V - \gamma_5 g_A, \quad (8)$$

$$\text{WM : } \quad F_2 = \mathcal{Z}_p - \mathcal{Z}_n - 1, \quad (9)$$

$$\text{PS : } \quad G_P = \frac{2 M_N^2 g_A}{m_\pi^2 - q_\mu^2}, \quad (10)$$

with vector and axial-vector coupling constants, $g_V = 1$ and $g_A = 1.27$, respectively, neutron and proton magnetic moments, $\mathcal{Z}_p = 2.793$ and $\mathcal{Z}_n = -1.913$, respectively, the pion mass $m_\pi = 138$ MeV, the vector mass $M_V = 840$ MeV and the axial-vector mass $M_A = 1$ GeV (cf. [22], except the m_π , which is taken as 138 MeV to be consistent with the parametrization of the RHF nuclear model from [23]). The labels in expressions (8)–(10) refer to the hadronic current contributions due to the leading

order (LO) and due to the inclusion of weak magnetism (WM) and pseudoscalar terms (PS). Furthermore, weak form factors (FF) are introduced via the following q_μ^2 -dependent terms as follows [15]:

$$g_V \rightarrow G_V(q_\mu^2) = \frac{g_V \left[1 - \frac{q_\mu^2 (\mathcal{Z}_p - \mathcal{Z}_n)}{4M_N^2} \right]}{\left(1 - \frac{q_\mu^2}{4M_N^2} \right) \left(1 - \frac{q_\mu^2}{M_V^2} \right)^2}, \quad (11a)$$

$$g_A \rightarrow G_A(q_\mu^2) = \frac{g_A}{\left(1 - \frac{q_\mu^2}{M_A^2} \right)^2}, \quad (11b)$$

$$F_2 \rightarrow F_2(q_\mu^2) = \frac{\mathcal{Z}_p - \mathcal{Z}_n - 1}{\left(1 - \frac{q_\mu^2}{4M_N^2} \right) \left(1 - \frac{q_\mu^2}{M_V^2} \right)^2}, \quad (11c)$$

$$G_P \rightarrow G_P(q_\mu^2) = \frac{2 M_N^2 G_A(q_\mu^2)}{m_\pi^2 - q_\mu^2}. \quad (11d)$$

In the following, we want to provide an expression for the hadron polarization tensor. Therefore, we rewrite the bosonic self-energy in the imaginary-time formalism, which is inserted in Eq (3) in the real-time formalism, in the following way [20, 24]:

$$\int \frac{d^4 p_2}{(2\pi)^4} \text{Tr} \{ G_2^<(p_2) \bar{V}_h^\mu G_4^>(p_4) V_h^\nu \} = 2 \text{Im} T \sum_n \int \frac{d^3 p_2}{(2\pi)^3} \frac{\text{Tr} \{ G_2(i\omega_n + \mu_2, \mathbf{p}_2) \bar{V}_h^\mu G_4(i\omega_m + i\omega_n + \mu_4, \mathbf{p}_2 + \mathbf{q}) V_h^\nu \}}{1 - \exp\{-(q_0 + \Delta\mu)/T\}} \quad (12)$$

$$\equiv \frac{2 \text{Im} \Pi^{\mu\nu}(i\omega_m - \Delta\mu, \mathbf{q})}{1 - \exp\{-(q_0 + \Delta\mu)/T\}}, \quad (13)$$

where the sum is over the fermionic Matsubara frequencies, $\omega_n = (2n+1)\pi T$ for $n = \{0, \pm 1, \dots\}$, $\Delta\mu = \mu_2 - \mu_4$ is the neutron-proton chemical potential difference, $\omega_m = 2m\pi T$ for $m = \{0, \pm 1, \dots\}$ is the bosonic Matsubara frequency and $\Pi^{\mu\nu}$ denotes the hadron polarization tensor in the imaginary-time formalism,

$$\Pi_{\mu\nu}(i\omega_m - \Delta\mu, \mathbf{q}) = T \sum_n \int \frac{d^3 p_2}{(2\pi)^3} \text{Tr} \{ G_2(i\omega_n + \mu_2, \mathbf{p}_2) \bar{V}_h^\mu G_4(i\omega_m + i\omega_n + \mu_4, \mathbf{p}_2 + \mathbf{q}) V_h^\nu \}, \quad (14)$$

with imaginary-time propagators,

$$G_a(i\omega_n + \mu_a, \mathbf{p}_a) = \frac{m_a - \not{p}_a}{E_a(\mathbf{p}_a)^2 - (i\omega_n + \mu_a)^2}, \quad (15)$$

where here $\not{p}_a = -(i\omega_n + \mu_a)\gamma^0 + \boldsymbol{\gamma} \cdot \mathbf{p}$, since in the imaginary-time formalism we switch to the Euclidean spacetime¹.

The hadron polarization tensor given by Eq. (14) can then be rewritten in terms of the trace with the summation over the Matsubara frequencies by defining the following quantity,

$$\tilde{\Pi}_{\mu\nu}(i\omega_m - \Delta\mu, \mathbf{q}) = T \sum_n \text{Tr} \{ G_2(i\omega_n + \mu_2, \mathbf{p}_2) \bar{V}_h^\mu G_4(i\omega_m + i\omega_n + \mu_4, \mathbf{p}_2 + \mathbf{q}) V_h^\nu \}, \quad (16)$$

such that Eq. (13) becomes,

$$\int \frac{d^4 p_2}{(2\pi)^4} \text{Tr} \{ G_2^<(p_2) \bar{V}_h^\mu G_4^>(p_4) V_h^\nu \} = 2 \int \frac{d^3 p_2}{(2\pi)^3} \frac{\text{Im} \tilde{\Pi}^{\mu\nu}(i\omega_m - \Delta\mu, \mathbf{q})}{1 - \exp\{-(q_0 + \Delta\mu)/T\}}. \quad (17)$$

¹ $\gamma^4 = i\gamma^0$ and $p_a^4 = i(\omega_n + \mu_a)$.

On the other hand, the left-hand side of Eq. (17) can be rewritten explicitly as follows,

$$\begin{aligned} \int \frac{d^4 p_2}{(2\pi)^4} \text{Tr} \{ G_2^<(p_2) \bar{V}_h^\mu G_4^>(p_4) V_h^\nu \} &= - \int \frac{d^4 p_2}{(2\pi)^2} \Lambda^{\mu\nu} f_2(p_2^0) (1 - f_4(p_2^0 + q_0)) \Theta(p_2^0) \Theta(p_2^0 + q_0) \\ &\quad \times \delta(p_2^2 - m_2^2) \delta((p_2 + q)^2 - m_4^2) \\ &= - \int \frac{d^3 p_2}{(2\pi)^2} \frac{\Lambda^{\mu\nu}}{4E_2 E_4} f_2(E_2) (1 - f_4(E_4)) \delta(q_0 + E_2 - E_4) , \end{aligned} \quad (18)$$

with the usage of Eqs. (4) and (5), and with $E_2 \equiv E_2(\mathbf{p}_2)$ and $E_4 \equiv E_4(\mathbf{p}_2 + \mathbf{q})$. In the last line we integrate over p_2^0 , using the Θ -function to remove the Dirac delta functions, and where the hadron tensor is given as follows,

$$\Lambda^{\mu\nu} = \text{Tr} \left\{ (\not{p}_2 + m_2) \bar{V}_h^\mu (\not{p}_4 + m_4) V_h^\nu \right\} . \quad (19)$$

By applying the following identity, $f_2(1 - f_4) = (f_2 - f_4)/[1 - \exp\{-(q_0 + \Delta\mu)/T\}]$, we cast Eq. (18) into the final form:

$$\int \frac{d^4 p_2}{(2\pi)^4} \text{Tr} \{ G_2^<(p_2) \bar{V}_h^\mu G_4^>(p_4) V_h^\nu \} = - \int \frac{d^3 p_2}{(2\pi)^2} \frac{\Lambda^{\mu\nu}}{4E_2 E_4} \frac{f_2(E_2) - f_4(E_4)}{1 - \exp\{-(q_0 + \Delta\mu)/T\}} \delta(q_0 + E_2 - E_4) . \quad (20)$$

The hadron tensor given in Eq. (16), which appears on the right-hand side of Eq. (17), needs to be calculated formally. Therefore, we make use of the formalism of Matsubara summation (note that $\exp\{\pm i\omega_m/T\} = 1$), which is based on the following prescription [20] (cf. Appendix C of Ref. [25]):

$$T \sum_n g(p_0 = i\omega_n + \mu_2) = \sum_i \text{Res}(g(p_0), z_i) \tilde{f}(p_0 - \mu_2) , \quad (21)$$

where $\tilde{f}(x) = [1 + \exp\{x/T\}]^{-1}$. We note that $g(p_0)$ is the meromorphic function of p_0 , which is regular on the vertical line, $\text{Re } p_0 = \mu_2$, decreasing faster than p_0^{-1} for $|p_0| \rightarrow \infty$. Note further that $\text{Res}(g(p_0), z_i)$ corresponds to the residue of g at the point z_i , which is a simple and isolated pole at $p_0 = z_i$, for which one obtains the following identity, $\text{Res}(g(p_0), z_i) = \lim_{p_0 \rightarrow z_i} (p_0 - z_i)g(p_0)$. Applying now Eq. (15) to Eq. (16), we obtain the following expression for the hadron polarization tensor ²:

$$\begin{aligned} \tilde{\Pi}_{\mu\nu}(\omega_0, \mathbf{q}) &= T \sum_n \frac{\tilde{\Lambda}^{\mu\nu}(p_0)}{(E_2 - p_0)(E_2 + p_0)(E_4 - (p_0 + \omega_0))(E_4 + p_0 + \omega_0)} \\ &= T \sum_n \frac{\tilde{\Lambda}^{\mu\nu}(p_0)}{4E_2 E_4} \left[\frac{1}{E_2 - p_0} + \frac{1}{E_2 + p_0} \right] \left[\frac{1}{E_4 - (p_0 + \omega_0)} + \frac{1}{E_4 + p_0 + \omega_0} \right] , \end{aligned} \quad (22)$$

and consequently the hadron tensor in the imaginary-time formalism is given by

$$\tilde{\Lambda}^{\mu\nu}(p_0) = \text{Tr} \left\{ [\gamma^0 p_0 - \boldsymbol{\gamma} \cdot \mathbf{p}_2 + m_2] \bar{V}_h^\mu [\gamma^0 (p_0 + \omega_0) - \boldsymbol{\gamma} \cdot \mathbf{p}_4 + m_4] V_h^\nu \right\} , \quad (23)$$

where $\omega_0 \equiv i\omega_m - \Delta\mu$. From Eq. (22), one can read off that we have 4 isolated poles at $p_0 = E_2$, $p_0 = -E_2$, $p_0 = E_4 - \omega_0$ and $p_0 = -E_4 - \omega_0$. Using Eq. (21) and collecting the terms with the same denominator, Eq. (22) becomes:

$$\begin{aligned} \tilde{\Pi}^{\mu\nu}(\omega_0, \mathbf{q}) &= \frac{1}{4E_2 E_4} \left\{ \frac{1}{\omega_0 + E_2 - E_4} \left[\tilde{\Lambda}^{\mu\nu}(E_2) f_2 - \tilde{\Lambda}^{\mu\nu}(E_4 - \omega_0) f_4 \right] \right. \\ &\quad + \frac{1}{\omega_0 - E_2 + E_4} \left[\tilde{\Lambda}^{\mu\nu}(-E_2) (1 - \bar{f}_2) - \tilde{\Lambda}^{\mu\nu}(-E_4 - \omega_0) (1 - \bar{f}_4) \right] \\ &\quad + \frac{1}{\omega_0 + E_2 + E_4} \left[-\tilde{\Lambda}^{\mu\nu}(E_2) f_2 + \tilde{\Lambda}^{\mu\nu}(-E_4 - \omega_0) (1 - \bar{f}_4) \right] \\ &\quad \left. + \frac{1}{\omega_0 - E_2 - E_4} \left[-\tilde{\Lambda}^{\mu\nu}(-E_2) (1 - \bar{f}_2) + \tilde{\Lambda}^{\mu\nu}(E_4 - \omega_0) f_4 \right] \right\} , \end{aligned} \quad (24)$$

where \bar{f}_a denotes the Fermi-Dirac distribution function of the antiparticle with $\bar{\mu}_a = -\mu_a$.

With the use of analytic continuation, $\omega_0 = i\omega_m - \Delta\mu \rightarrow q_0 + i\eta$, we can obtain the real-time polarization tensor, which is required in the calculations of the neutrino absorption rate, and we come naturally back to the Minkowski spacetime. The only term which will contribute in the considered process (1), after we take the imaginary part, is the first term in Eq. (24) with square brackets as was discussed in Refs. [24, 26] with the kinematic constraint that $q_\mu^2 \leq (m_2 - m_4)^2$. By applying now the identity with the Cauchy principle value³, performing the analytic continuation and taking the imaginary part, we obtain the following final expression for the hadron polarization tensor,

$$\text{Im } \tilde{\Pi}^{\mu\nu}(q_0, q) = -\pi \frac{f_2 - f_4}{4E_2 E_4} \Lambda^{\mu\nu} \delta(q_0 + E_2 - E_4), \quad (25)$$

where we note that the imaginary part is not taken over $\Lambda^{\mu\nu}$, given by Eq. (19) [24], which is the requirement to connect the real- and imaginary-time expressions of the inserted bosonic self-energy. Implementing the above result into Eq. (17) together with Eq. (20), we confirm that this relation is true.

By combining Eq. (17) for bosonic self-energy and Eq. (4) for particle 3 in Eq. (2) together with Eq. (3), we obtain the following neutrino absorption rate, i.e. the neutrino opacity being the inverse of the neutrino mean-free path, $\Gamma(E_1) = 1/\lambda_1$:

$$\begin{aligned} \Gamma(E_1) = & -\frac{G_F^2 C^2}{32\pi^3} \int \frac{d^3 p_3}{E_1 E_3} \int \frac{d^3 p_2}{(2\pi)^3} [1 - f_3(E_3)] \\ & \times \frac{L_{\mu\nu} \text{Im } \tilde{\Pi}^{\mu\nu}(q_0, \mathbf{q})}{1 - \exp\{-(q_0 + \Delta\mu)/T\}} \end{aligned} \quad (26)$$

where the lepton tensor,

$$L_{\mu\nu} = \text{Tr} \left\{ \not{p}_1 \bar{V}_\mu (\not{p}_3 + m_3) V_\nu \right\}, \quad (27)$$

does not factor out of the integral over p_2 in expression (26), which is the very essence of the RHF approach, differing from commonly employed mean-field models, in which the lepton tensor factorizes [9, 24]. More details on the decomposition of $L_{\mu\nu}$ will be given below in Sec. III.

Finally, Eq. (26) can be cast in the following differential form

$$\begin{aligned} \frac{d\Gamma(E_1)}{dE_3 d\Omega_{13}} = & -\frac{G_F^2 C^2}{32\pi^3} \frac{p_3}{E_1} \frac{1 - f_3(E_3)}{1 - \exp\{-(q_0 + \Delta\mu)/T\}} \\ & \times \int \frac{d^3 p_2}{(2\pi)^3} L_{\mu\nu} \text{Im } \tilde{\Pi}^{\mu\nu}(q_0, \mathbf{q}), \end{aligned} \quad (28)$$

where we change the integration variable from p_3 to E_3 , where $E_3^2 = p_3^2 + m_3^2$, and $d\Omega_{13} = d\mu_{13} d\phi_{13}$, where

³ $(x \pm i\eta)^{-1} = \mathcal{P}x^{-1} \mp i\pi\delta(x)$.

$\mu_{13} = \cos\theta_{13}$ is the cosine of the relative momentum angle between particles 1 and 3 and ϕ_{13} is their azimuthal angle. A detailed discussion of the derivation of the above expressions within the mean-field approximation and how they are related to the free theory is provided in [24].

III. NEUTRINO ABSORPTION RATES WITHIN THE RELATIVISTIC HARTREE-FOCK TREATMENT

In this section, we lay out the formalism for the relativistic Hartree-Fock approximation [19, 27] and show how the expression describing the neutrino opacity compared to the RMF approximation differs. Therefore, the nucleons are put on-shell, i.e. $p_a^0 = E_a(p_a)$, and the nucleon self-energy is decomposed into scalar Σ_a^S , time-like Σ_a^0 and vector Σ_a^V components as follows [23],

$$\Sigma_a(p_a) = \Sigma_a^S(p_a) + \gamma^0 \Sigma_a^0(p_a) + \boldsymbol{\gamma} \cdot \hat{\mathbf{p}}_a \Sigma_a^V(p_a), \quad (29)$$

where $\hat{\mathbf{p}}_a \equiv \mathbf{p}_a/|\mathbf{p}_a|$ is the unit momentum vector and in the following we use $p_a \equiv |\mathbf{p}_a|$. We note that momentum-dependence is explicitly included, unlike within the RMF approximation, as it appears on account of the specific form of the Fock diagram (see Appendix A). As a consequence, the nucleon masses, m_a , momenta, \mathbf{p}_a , and dispersion relations, E_a , are expressed as effective (dressed) quantities as follows,

$$m_a^*(p_a) = m_a + \Sigma_a^S(p_a), \quad (30a)$$

$$\mathbf{p}_a^*(p_a) = \mathbf{p}_a + \hat{\mathbf{p}}_a \Sigma_a^V(p_a), \quad (30b)$$

$$E_a^*(p_a) = E_a(p_a) - \Sigma_a^0(p_a), \quad (30c)$$

where $E_a^*(p_a) = \sqrt{\mathbf{p}_a^{*2}(p_a) + m_a^{*2}(p_a)}$. Details about the standard RHF model employed here, based on the exchange of σ , ω , ρ and π mesons, are given in Appendix A, closely following Ref. [23], including the explicit expressions for the nucleon self-energies.

Since according to electroweak kinematics, we have $\mathbf{p}_4 = \mathbf{p}_2 + \mathbf{q}$ and we only integrate over p_2 (not p_4), $E_4^*(p_4)$ can be expressed as follows

$$\begin{aligned} E_4^*(p_2, q) = & \left[|\mathbf{p}_2 + \mathbf{q}|^2 + \Sigma_4^V(|\mathbf{p}_2 + \mathbf{q}|)^2 \right. \\ & \left. + 2|\mathbf{p}_2 + \mathbf{q}| \Sigma_4^V(|\mathbf{p}_2 + \mathbf{q}|) + m_4^{*2}(|\mathbf{p}_2 + \mathbf{q}|) \right]^{1/2}, \end{aligned} \quad (31)$$

where

$$\begin{aligned} p_4 = |\mathbf{p}_4| = |\mathbf{p}_2 + \mathbf{q}| & = \sqrt{(\mathbf{p}_2 + \mathbf{q})^2} \\ & = \sqrt{p_2^2 + q^2 + 2p_2 q \mu_{24}}. \end{aligned} \quad (32)$$

Consequently, the nucleon self-energies for the particle 4 depend explicitly on p_2 , q and μ_{24} , which is the cosine of the momentum angle between the particles 2 and 4.

In the following, we introduce the effective 4-momentum transfer, $\tilde{q}^\mu = (\tilde{q}_0, \tilde{\mathbf{q}})$, where

$$\tilde{q}_0 = q_0 + \Sigma_2^0(p_2) - \Sigma_4^0(p_4) \equiv q_0 + \Delta\Sigma^0, \quad (33a)$$

$$\tilde{\mathbf{q}} = \mathbf{q} - \hat{\mathbf{p}}_2 \Sigma_2^V(p_2) + \hat{\mathbf{p}}_4 \Sigma_4^V(p_4) \equiv \mathbf{q} - \Delta \Sigma^V \quad (33b)$$

with the following 4-vector $\Delta \Sigma^\mu = (\Delta \Sigma^0, -\Delta \Sigma^V)$. Moreover, $\tilde{q}^\mu = p_4^{*\mu} - p_2^{*\mu}$, where $p_a^{*\mu} = (E_a^*(p_a), \mathbf{p}_a^*(p_a))$. For numerical purposes, we provide the explicit form of $\tilde{q}_\mu^2 = \tilde{q}_0^2 - \tilde{\mathbf{q}}^2$, where

$$\tilde{q}_0^2 = (q_0 + \Delta \Sigma^0)^2, \quad (34a)$$

$$\tilde{\mathbf{q}}^2 = \mathbf{q}^2 + (\Delta \Sigma^V)^2 - 2 \mathbf{q} \cdot \Delta \Sigma^V, \quad (34b)$$

with

$$(\Delta \Sigma^V)^2 = (\Sigma_2^V)^2 + (\Sigma_4^V)^2 - \frac{2 \Sigma_2^V \Sigma_4^V}{p_4} (p_2 + q \mu_{24}), \quad (34c)$$

$$\mathbf{q} \cdot \Delta \Sigma = q \mu_{24} \Sigma_2^V - \frac{p_2 q \mu_{24} + q^2}{p_4} \Sigma_4^V. \quad (34d)$$

Following the approach presented in Ref. [24], how to replace the bare quantities in the free theory with the corresponding ones in the interacting theory in Eq. (25), e.g., within the mean-field approach, we note that the analog also holds within the RHF approximation. Therefore, in order to rewrite the differential absorption rate given by Eq. (28) within the RHF approximation, we replace the bare quantities with the effective ones given in (30), make a substitution: $q^\mu \rightarrow \tilde{q}^\mu$ and insert Eq. (25), in order to obtain

$$\begin{aligned} \frac{d\Gamma(E_1)}{dE_3 d\Omega_{13}} &= \frac{G_F^2 C^2 p_3}{32\pi^2 E_1} \frac{1 - f_3(E_3)}{1 - \exp\{-(q_0 + \Delta\mu)/T\}} \\ &\times \int \frac{d^3 p_2}{(2\pi)^3} \delta(\tilde{q}_0 + E_2^*(p_2) - E_4^*(p_4)) \\ &\times [f_2(E_2) - f_4(E_4)] \frac{L_{\mu\nu} \Lambda^{\mu\nu}}{4E_2^*(p_2)E_4^*(p_4)}, \quad (35) \end{aligned}$$

with

$$\begin{aligned} \Lambda^{\mu\nu} &= \text{Tr} \left\{ \left(\not{p}_2^*(p_2) + m_2^*(p_2) \right) \left[\gamma^\mu (G_V(q_\mu^2) - G_A(q_\mu^2) \gamma_5) \right. \right. \\ &\quad \left. \left. - F_2(q_\mu^2) \frac{i\sigma^{\mu\alpha} \tilde{q}_\alpha}{2M_N} + \frac{G_P(q_\mu^2)}{M_N} \gamma_5 \tilde{q}^\mu \right] \right. \\ &\quad \times \left(\not{p}_4^*(p_4) + m_4^*(p_4) \right) \left[\gamma^\nu (G_V(q_\mu^2) - G_A(q_\mu^2) \gamma_5) \right. \\ &\quad \left. \left. + F_2(q_\mu^2) \frac{i\sigma^{\nu\beta} \tilde{q}_\beta}{2M_N} - \frac{G_P(q_\mu^2)}{M_N} \gamma_5 \tilde{q}^\nu \right] \right\}, \quad (36) \end{aligned}$$

where both lepton and hadron tensors appear under the integral over p_2 and we note that in the denominator of the term with $F_2(q_\mu^2)$, there should be M_N , not M_p as was stated in Ref. [24]. Note further that the single-particle energy, E_a , contained in the Fermi-Dirac distributions has to be determined via solutions of Eq. (30c), which makes the distributions explicitly depend on the dressed quantities in (30). In comparison with the RMF

approach the essential difference in the RHF treatment arises due to the explicit momentum-dependent nucleon self-energies, which will be shown further below. In the following, we omit the arguments in the effective quantities given in (30) for clarity.

In the RHF framework, the contraction of the lepton and hadron tensors can be written as follows [24],

$$\begin{aligned} L_{\mu\nu} \Lambda^{\mu\nu} &= \sum_{i \in \mathcal{A}} C_i [L_L \Lambda_L^i + L_Q \Lambda_Q^i - 2L_{M+} \Lambda_{M+}^i \\ &\quad - 2L_{M-} \Lambda_{M-}^i + 2L_{T+} \Lambda_{T+}^i + 2L_{T-} \Lambda_{T-}^i], \quad (37) \end{aligned}$$

with the following definitions,

$$\mathcal{A} = \{V, A, T, P, VA, VT, AT, VP, AP, TP\}, \quad (38a)$$

and

$$\begin{aligned} C_i &= \{g_V^2, g_A^2, F_2^2, G_P^2, g_V g_A, g_V F_2, g_A F_2, \\ &\quad g_V G_P, g_A G_P, F_2 G_P\}, \quad (38b) \end{aligned}$$

where \mathcal{A} contains all vector (V), axial-vector (A), tensor (T) and pseudoscalar (P) components, as well as their combinations with the corresponding coupling constants in C_i , which can be replaced by the form factors as given by (11).

In the following, we choose the 4-momentum transfer, $\tilde{q}^\mu = (\tilde{q}_0, 0, 0, \tilde{q})$, aligned with the z-axis and $\tilde{n}^\mu = (\tilde{q}, 0, 0, \tilde{q}_0)$ orthogonal to \tilde{q}^μ , where $\tilde{q} = \sqrt{\tilde{\mathbf{q}}^2}$ with $\tilde{\mathbf{q}}$ given by Eq. (34b). Using these vectors, we then build the following set of projectors [24]. First, the *transverse projector* (orthogonal to both \tilde{q}^μ and \tilde{n}^μ) is given as follows,

$$\begin{aligned} P_{\mu\nu}^{T+} &= g_{\mu\nu} - \frac{\tilde{q}_\mu \tilde{q}_\nu}{\tilde{q}_\mu^2} - \frac{\tilde{n}_\mu \tilde{n}_\nu}{\tilde{n}_\mu^2} \\ &= g_{\mu\nu} + \frac{\tilde{n}_\mu \tilde{n}_\nu - \tilde{q}_\mu \tilde{q}_\nu}{\tilde{q}_\mu^2}, \quad (39) \end{aligned}$$

where $\tilde{n}_\mu^2 = -\tilde{q}_\mu^2$, and the *longitudinal projectors* along \tilde{q}^μ and \tilde{n}^μ , respectively, are

$$P_{\mu\nu}^L = \frac{\tilde{n}_\mu \tilde{n}_\nu}{\tilde{n}_\mu^2} = -\frac{\tilde{n}_\mu \tilde{n}_\nu}{\tilde{q}_\mu^2}, \quad (40a)$$

$$P_{\mu\nu}^Q = \frac{\tilde{q}_\mu \tilde{q}_\nu}{\tilde{q}_\mu^2}. \quad (40b)$$

We further define the following projectors:

$$P_{\mu\nu}^{M\pm} = \frac{\tilde{q}_\mu \tilde{n}_\nu \pm \tilde{n}_\mu \tilde{q}_\nu}{\tilde{q}_\mu^2}, \quad (41a)$$

$$P_{\mu\nu}^{T-} = \epsilon_{\mu\nu\rho\sigma} \frac{\tilde{q}^\rho \tilde{n}^\sigma}{\tilde{q}_\mu^2}. \quad (41b)$$

The only non-zero contractions of these projectors are

$$P_{\mu\nu}^L P_L^{\mu\nu} = 1, \quad (42a)$$

$$P_{\mu\nu}^Q P_Q^{\mu\nu} = 1 , \quad (42b)$$

$$P_{\mu\nu}^{M\pm} P_{M\pm}^{\mu\nu} = -2 , \quad (42c)$$

$$P_{\mu\nu}^{T\pm} P_{T\pm}^{\mu\nu} = 2 . \quad (42d)$$

From these considerations it follows that any rank-2 tensor, $T_{\mu\nu}$, can be decomposed as follows,

$$\begin{aligned} T_{\mu\nu} = & T_Q P_{\mu\nu}^Q + T_L P_{\mu\nu}^L + T_{M+} P_{\mu\nu}^{M+} + T_{M-} P_{\mu\nu}^{M-} \\ & + T_{T+} P_{\mu\nu}^{T+} + T_{T-} P_{\mu\nu}^{T-} , \end{aligned} \quad (43)$$

where the components are obtained by using the following relations,

$$T_Q = P_Q^{\mu\nu} T_{\mu\nu} , \quad (44a)$$

$$T_L = P_L^{\mu\nu} T_{\mu\nu} , \quad (44b)$$

$$T_{M\pm} = -\frac{1}{2} P_{M\pm}^{\mu\nu} T_{\mu\nu} , \quad (44c)$$

$$T_{T\pm} = \frac{1}{2} P_{T\pm}^{\mu\nu} T_{\mu\nu} . \quad (44d)$$

Let us first consider the lepton tensor given in Eq. (27) for the two processes (1), $\nu_e + n \rightarrow e^- + p$ and $\bar{\nu}_e + p \rightarrow e^+ + n$, which takes the following form:

$$L_{\mu\nu} = \text{Tr} \left\{ \not{p}_1 \gamma_\mu (1 \mp \gamma_5) (\not{p}_3 \pm m_3) \gamma_\nu (1 \mp \gamma_5) \right\} \quad (45)$$

$$\begin{aligned} = & 8 [2p_{1\mu} p_{1\nu} + p_1^\alpha q_\alpha g_{\mu\nu} - (p_{1\mu} q_\nu + p_{1\nu} q_\mu) \\ & \pm i \epsilon_{\mu\nu\alpha\beta} p_1^\alpha q^\beta] , \end{aligned} \quad (46)$$

where the upper sign is for neutrinos and the lower sign is for antineutrinos. All decomposed components will depend on the following 4-momentum contractions:

$$p_1 \cdot q = \frac{q_\mu^2 - m_3^2}{2} , \quad (47a)$$

$$p_1 \cdot \tilde{q} = p_1 \cdot q + p_1 \cdot \Delta\Sigma , \quad (47b)$$

$$p_1 \cdot \tilde{n} = \frac{1}{\tilde{q}} \left[-E_1 \tilde{q}_\mu^2 + \frac{\tilde{q}_0}{2} (q_\mu^2 - m_3^2) + \tilde{q}_0 (p_1 \cdot \Delta\Sigma) \right] , \quad (47c)$$

$$\tilde{n} \cdot q = \tilde{q} q_0 - \tilde{q}_0 q , \quad (47d)$$

$$q \cdot \tilde{q} = q_0 \tilde{q}_0 - q \tilde{q} , \quad (47e)$$

along with $\tilde{q} \cdot \tilde{n} = 0$, where

$$\begin{aligned} p_1 \cdot \Delta\Sigma = & E_1 \Delta\Sigma^0 + \frac{\mathbf{p}_1 \cdot \mathbf{p}_2}{p_2} \Sigma_2^V \\ & - \frac{\mathbf{p}_1 \cdot \mathbf{p}_2 + \mathbf{p}_1 \cdot \mathbf{q}}{p_4} \Sigma_4^V , \end{aligned} \quad (48a)$$

$$\mathbf{p}_1 \cdot \mathbf{q} = E_1 q_0 - p_1 \cdot q , \quad (48b)$$

$$\mathbf{p}_1 \cdot \mathbf{p}_2 = p_1^1 p_2^1 + p_1^2 p_2^2 + p_1^3 p_2^3 , \quad (48c)$$

and the momentum components are easily found in polar coordinates⁴. Then, the components of the lepton tensor are:

$$L_L = \frac{8}{\tilde{q}_\mu^2} \left[-2(p_1 \cdot \tilde{n})^2 + 2(p_1 \cdot \tilde{n})(q \cdot \tilde{n}) + q_\mu^2 (p_1 \cdot q) \right] , \quad (49a)$$

$$L_Q = \frac{8}{\tilde{q}_\mu^2} \left[2(p_1 \cdot \tilde{q})^2 - 2(p_1 \cdot \tilde{q})(q \cdot \tilde{q}) + q_\mu^2 (p_1 \cdot q) \right] , \quad (49b)$$

$$L_{M+} = \frac{8}{\tilde{q}_\mu^2} \left[(p_1 \cdot \tilde{q})(q \cdot \tilde{n}) + (p_1 \cdot \tilde{n})(q \cdot \tilde{q}) - 2(p_1 \cdot \tilde{q}) \right] , \quad (49c)$$

$$L_{M-} = \mp \frac{8i}{\tilde{q}_\mu^2} e^{\mu\nu\alpha\beta} \tilde{n}_\mu p_{1\nu} \tilde{q}_\alpha q_\beta = 0 , \quad (49d)$$

$$\begin{aligned} L_{T+} = & \frac{8}{\tilde{q}_\mu^2} \left[(p_1 \cdot \tilde{n})^2 - (p_1 \cdot \tilde{n})(q \cdot \tilde{n}) + (p_1 \cdot \tilde{q})(q \cdot \tilde{q}) \right. \\ & \left. - (p_1 \cdot \tilde{q}) \right] , \end{aligned} \quad (49e)$$

$$L_{T-} = \pm \frac{8i}{\tilde{q}_\mu^2} \left[(p_1 \cdot \tilde{n})(q \cdot \tilde{q}) - (q \cdot \tilde{n})(p_1 \cdot \tilde{q}) \right] , \quad (49f)$$

where the upper sign is for neutrinos and the lower sign is for antineutrinos.

Moving on to the hadron tensor, we first list the following 4-momentum contractions used in the calculations:

$$p_2^* \cdot \tilde{q} = E_2^* E_4^* - p_2^* \tilde{q} \mu_{24} - E_2^{*2} , \quad (50a)$$

$$p_2^* \cdot \tilde{n} = E_2^* \tilde{q} - p_2^* \tilde{q}_0 \mu_{24} . \quad (50b)$$

Then, the non-zero components of the hadron tensor given in Eq. (36) are as follows:

1. Vector:

$$\begin{aligned} \Lambda_Q^V = & \frac{4}{\tilde{q}_\mu^2} \left[- (m_2^{*2} - m_2^* m_4^*) \tilde{q}_\mu^2 + 2(p_2^* \cdot \tilde{q})^2 \right. \\ & \left. + (p_2^* \cdot \tilde{q}) \tilde{q}_\mu^2 \right] , \end{aligned} \quad (51a)$$

$$\begin{aligned} \Lambda_L^V = & -\frac{4}{\tilde{q}_\mu^2} \left[(m_2^{*2} - m_2^* m_4^*) \tilde{q}_\mu^2 + (p_2^* \cdot \tilde{q}) \tilde{q}_\mu^2 \right. \\ & \left. + 2(p_2^* \cdot \tilde{n})^2 \right] , \end{aligned} \quad (51b)$$

$$\Lambda_{T+}^V = \frac{1}{2} \left\{ 8 \left[-m_2^{*2} + 2m_2^* m_4^* - (p_2^* \cdot \tilde{q}) \right] - \Lambda_L^V - \Lambda_Q^V \right\} , \quad (51c)$$

$$\Lambda_{M+}^V = -\frac{4}{\tilde{q}_\mu^2} \left[2(p_2^* \cdot \tilde{q})(p_2^* \cdot \tilde{n}) + (p_2^* \cdot \tilde{n}) \tilde{q}_\mu^2 \right] . \quad (51d)$$

⁴ $p_a^1 = p_a \sin \theta_a \cos \phi_a$, $p_a^2 = p_a \sin \theta_a \sin \phi_a$, $p_a^3 = p_a \cos \theta_a$, where we define $\theta_1 \equiv \theta_{13}$, $\theta_2 \equiv \theta_{24}$, $\phi_1 \equiv \phi_{13}$ and $\phi_2 \equiv \phi_{24}$.

2. Axial-vector:

$$\Lambda_Q^A = \frac{4}{\tilde{q}_\mu^2} \left[- (m_2^{*2} + m_2^* m_4^*) \tilde{q}_\mu^2 + 2(p_2^* \cdot \tilde{q})^2 + (p_2^* \cdot \tilde{q}) \tilde{q}_\mu^2 \right], \quad (52a)$$

$$\Lambda_L^A = - \frac{4}{\tilde{q}_\mu^2} \left[(m_2^{*2} + m_2^* m_4^*) \tilde{q}_\mu^2 + (p_2^* \cdot \tilde{q}) \tilde{q}_\mu^2 + 2(p_2^* \cdot \tilde{n})^2 \right], \quad (52b)$$

$$\Lambda_{T+}^A = \frac{1}{2} \left\{ 8 [-m_2^{*2} - 2m_2^* m_4^* - (p_2^* \cdot \tilde{q})] - \Lambda_L^A - \Lambda_Q^A \right\}, \quad (52c)$$

$$\Lambda_{M+}^A = - \frac{4}{\tilde{q}_\mu^2} [2(p_2^* \cdot \tilde{q})(p_2^* \cdot \tilde{n}) + (p_2^* \cdot \tilde{n}) \tilde{q}_\mu^2]. \quad (52d)$$

3. Tensor:

$$\Lambda_L^T = \frac{1}{M_N^2} \left\{ (m_2^{*2} + m_2^* m_4^*) \tilde{q}_\mu^2 - (p_2^* \cdot \tilde{q}) [\tilde{q}_\mu^2 + 2(p_2^* \cdot \tilde{q})] + 2(p_2^* \cdot \tilde{n})^2 \right\}, \quad (53a)$$

$$\Lambda_{T+}^T = \frac{1}{2} \left\{ \frac{1}{M_N^2} [(m_2^{*2} + 3m_2^* m_4^*) \tilde{q}_\mu^2 - 3(p_2^* \cdot \tilde{q}) \tilde{q}_\mu^2 - 4(p_2^* \cdot \tilde{q})^2] - \Lambda_L^T \right\}. \quad (53b)$$

4. Pseudoscalar:

$$\Lambda_Q^P = 4 \frac{\tilde{q}_\mu^2}{M_N^2} [m_2^{*2} - m_2^* m_4^* + (p_2^* \cdot \tilde{q})]. \quad (54)$$

5. Vector axial-vector:

$$\Lambda_{T-}^{VA} = -8i(p_2^* \cdot \tilde{n}). \quad (55)$$

6. Vector tensor:

$$\Lambda_L^{VT} = -4\Delta(p_2^* \cdot \tilde{q}) + 4 \frac{m_2^*}{M_N} \tilde{q}_\mu^2, \quad (56a)$$

$$\Lambda_{T+}^{VT} = -6\Delta(p_2^* \cdot \tilde{q}) + 6 \frac{m_2^*}{M_N} \tilde{q}_\mu^2 - \frac{1}{2} \Lambda_L^{VT}, \quad (56b)$$

$$\Lambda_{M+}^{VT} = -2\Delta(p_2^* \cdot \tilde{n}), \quad (56c)$$

where $\Delta = (m_4^* - m_2^*)/M_N$ and we note here that the denominator of Δ contains M_N , not M_2^* as given in the denominator in Ref. [24].

7. Axial-vector tensor:

$$\Lambda_{T-}^{AT} = -4i \left(\Delta + 2 \frac{m_2^*}{M_N} \right) (p_2^* \cdot \tilde{n}). \quad (57)$$

8. Axial-vector pseudoscalar:

$$\Lambda_Q^{AP} = 8 \left[\Delta(p_2^* \cdot \tilde{q}) - \tilde{q}_\mu^2 \frac{m_2^*}{M_N} \right], \quad (58a)$$

$$\Lambda_{M+}^{AP} = -4\Delta(p_2^* \cdot \tilde{n}). \quad (58b)$$

When considering the process $\bar{\nu}_e + p \rightarrow e^+ + n$, the only modification required in the hadron tensor (Eq. (36)) is the interchange of the labels $2 \leftrightarrow 4$ in the non-zero components.

Before writing the expression for neutrino absorption rate within the RHF approximation, we note that the kinematics of the incoming and outgoing leptons can be expressed in terms of the 4-momentum transfer introduced above, i.e., the energy and 3-momentum transfer for a given incoming neutrino energy, E_1 :

$$q_0 = E_1 - E_3, \quad (59)$$

$$q = \sqrt{E_1^2 + p_3^2 - 2E_1 p_3 \mu_{13}}, \quad (60)$$

where $p_3 = \sqrt{E_3^2 - m_3^2}$. From Eq. (59), considering the allowed range for $E_3 \in [m_3, \infty)$, one finds that q_0 is constrained by $-\infty < q_0 < E_1 - m_3$. Moreover, from Eq. (60), taking the extreme values of $\mu_{13} = \pm 1$, the momentum transfer q satisfies $|E_1 - p_3| < q < E_1 + p_3$.

Finally, since the contracted 4-momenta given in Eqs. (47) and (50) within the RHF approximation involve all the possible angles and integration variables, i.e. q_0 (it originates from E_3 via Eq. (59)), μ_{13} , μ_{24} , ϕ_{13} , ϕ_{24} and p_2 , the neutrino opacity has the following general expression obtained from Eq. (35):

$$\Gamma(E_1) = \frac{G_F^2 C^2}{32\pi^2} \int_{-\infty}^{E_1 - m_3} dq_0 \frac{p_3}{E_1} \frac{1 - f_3(E_3)}{1 - \exp\{-(q_0 + \Delta\mu)/T\}} \int_{-1}^1 d\mu_{13} \int_0^{2\pi} d\phi_{13} \int_{-1}^1 d\mu_{24} \int_0^{2\pi} d\phi_{24} \times \int_0^\infty \frac{dp_2}{(2\pi)^3} p_2^2 \delta(\tilde{q}_0 + E_2^*(p_2) - E_4^*(p_4)) [f_2(E_2) - f_4(E_4)] \frac{L_{\mu\nu} \Lambda^{\mu\nu}}{4E_2^*(p_2)E_4^*(p_4)}. \quad (61)$$

The standard form of neutrino opacity within the RMF

approximation with the integrals over q_0 and q is given

in Appendix B. The last modification, which one has to apply in case of the process $\bar{\nu}_e + p \rightarrow e^+ + n$, is the following replacement: $f_3 \rightarrow \bar{f}_3$, i.e. $\mu_3 \rightarrow -\mu_3$.

IV. COMPARING THE NEUTRINO OPACITY WITHIN RHF AND RMF APPROACHES

In the following, we will evaluate the expressions (35) and (61) numerically. Therefore, we choose two representative conditions, which we select from Ref. [15]. We list these conditions in Table I, henceforth denoted as A and B, in terms of temperature T , baryon density n_B (in units of the nuclear saturation density n_0), electron and muon abundances, Y_e and Y_μ (satisfying the local charge neutrality condition, $Y_p = Y_e + Y_\mu$), and electron and muon chemical potentials, μ_e and μ_μ , respectively. Furthermore, we provide the corresponding thermodynamic chemical potentials, μ_n and μ_p , and the RMF scalar self-energy, Σ^S and zero-component (time-like) self-energies, Σ_n^0 and Σ_p^0 , distinguishing neutrons and protons, in Table II. In the following, we distinguish the RHF nuclear model from common RMF parameterizations. To this end, we select the TMA [28], NL3 [29] and DD2 [30, 31] RMF models. The former two possess non-linearity via meson-meson interactions and the latter one contains density-dependent meson-nucleon couplings, fitted to Dirac-Brueckner-Hartree-Fock calculations (further details are given in Ref. [30]). All of these RMF parameterizations employ σ , ω and ρ meson interaction channels, and omit the presence of nuclear clusters at sub-saturation density [32, 33]. Bulk nuclear matter properties for TMA, NL3 and DD2 can be found in Ref. [34] and references therein. We note here that these nuclear EOS have been commonly employed in astrophysical studies of core-collapse supernovae and binary neutron star mergers [35–37].

For further evaluation and implementation of the RHF and RMF models (cf. conditions A and B in Tables I and II), in addition to temperature, we ensure identical baryon density and proton fraction, hence the different values of the neutron and proton chemical potentials and the different values of the self-energies for RHF, TMA, NL3 and DD2. We note in particular the different magnitudes of $\Sigma_n^0 - \Sigma_p^0$. We will return to this aspect further below, when discussing the neutrino opacity. We note further that within the selected RMF models, neutron and proton scalar self-energies are identical, which is attributed to the absence of the isovector-scalar δ -meson [38]. Within RHF, by construction, the neutron and proton scalar self-energies are different, as detailed in Appendix A.

We emphasize here that the neutron and proton chemical potentials, as well as the self-energies, differ from the values used in Ref. [15], due to the different nuclear matter model. Nevertheless, these conditions are taken from simulations of self-consistent neutrino-driven core-collapse supernova explosions from

TABLE I. Two selected conditions [15], listing temperature T , baryon density n_B , lepton fractions and chemical potentials for electrons and muons, Y_e, Y_μ, μ_e and μ_μ , respectively. Except the lepton fractions and n_B , where the latter is in units of the saturation density n_0 , all quantities are given in units of MeV.

Model	T	n_B/n_0	Y_e	Y_μ	μ_e	μ_μ
A	38.3	0.406	0.13	0.040	83	67
B	15.2	0.053	0.11	0.002	45	38

TABLE II. Thermodynamic neutron and proton chemical potentials, μ_n and μ_p , as well as scalar and time-like components of the self-energy, Σ^S and Σ^0 for RHF and a selection of RMF models, for the two representative conditions A and B (see Table I). All quantities are given in units of MeV. We note here the different saturation densities: $n_0^{\text{RHF/RMF}^*} = 0.150 \text{ fm}^{-3}$, $n_0^{\text{TMA}} = 0.147 \text{ fm}^{-3}$, $n_0^{\text{NL3}} = 0.148 \text{ fm}^{-3}$ and $n_0^{\text{DD2}} = 0.149 \text{ fm}^{-3}$.

Model	μ_n	μ_p	Σ^S	Σ_n^0	Σ_p^0
RHF	898.0	822.9	—†	—†	—†
RMF (TMA)	896.4	814.4	−153.58	128.43	113.61
A RMF (NL3)	900.0	811.7	−157.57	135.33	114.38
RMF (DD2)	904.8	811.3	−202.40	180.83	155.14
RMF*	897.9	823.1	−173.72	147.46	140.26
RHF	915.7	879.8	—†	—†	—†
RMF (TMA)	915.0	878.8	−21.86	17.28	15.00
B RMF (NL3)	914.3	877.2	−23.33	17.91	14.69
RMF (DD2)	915.7	876.1	−33.43	29.05	23.37
RMF*	915.4	880.4	−23.92	19.33	18.23

† Momentum-dependent RHF self-energies are listed in Tables (IV) and (V) for conditions A and B (see also Fig. 2).

the Garching group [39], featuring the nuclear EOS of Lattimer & Swesty [40] and where muonic neutrino interactions are taken into account self-consistently, with the treatment of charged-current muonic processes at the mean-field level.

Furthermore, we introduce another RMF model, which is the reduction of the RHF model, henceforth denoted as RMF*, based on the same mesons (σ , ω , ρ) as the RHF, except pions and tensor terms, which vanish at the mean-field level as explained in Appendix A and are omitted by design within all RMF models. In order to achieve this reduction, we take all the same rest masses and coupling constants as given in Appendix A and refit the σ and ω coupling constants to obtain at $n_0^{\text{RHF}} = 0.15 \text{ fm}^{-3}$ the binding energy $E_B = -15.75 \text{ MeV}$, which after the normalization are given by $g_\sigma^2/4\pi = 6.19$ and $g_\omega^2/4\pi = 15.0$. The resulting neutron and proton chemical potentials, together with the self-energies, are listed in Table II. Details about the comparison between RHF and RMF* are given in Sec. V, while details about the RHF model used here are given in Appendix A, together with the numerical evaluation of the momentum-dependent self-energies, as shown in Fig. 2 for both conditions A (left panel) and B (right panel). The numerical values are listed in Ta-

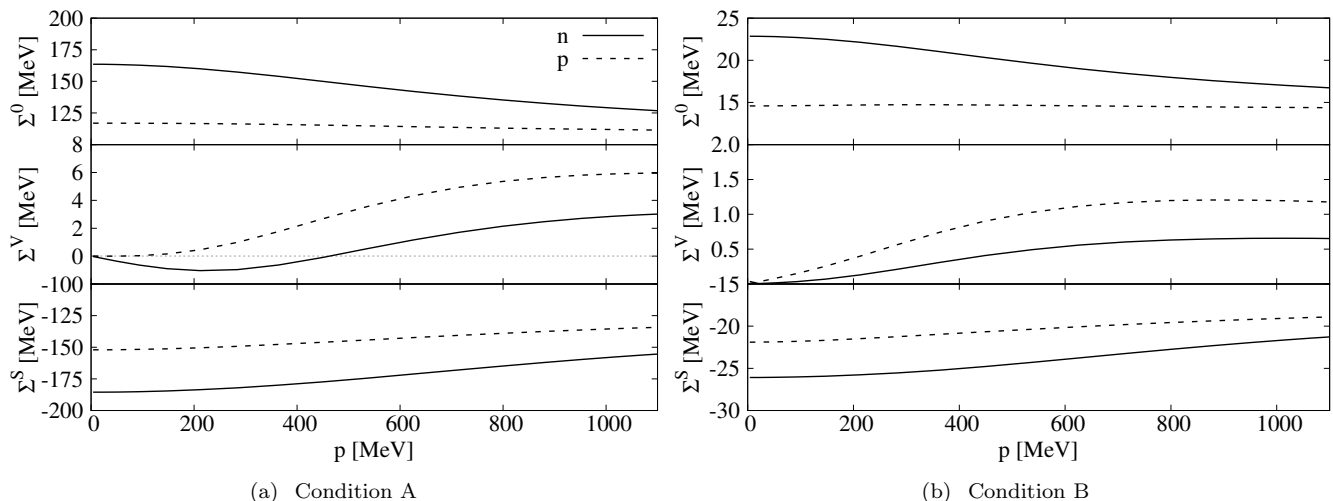


FIG. 2. Hartree-Fock nucleon self-energy components (black lines): scalar Σ^S , time-like Σ^0 and space-like (vector) Σ^V , with respect to momentum p for neutrons (solid lines) and protons (dashed lines), at two representative conditions A (left panel) and B (right panel) listed in Tables I and II.

bles IV and V in Appendix D.

One of the complications that arise within the RHF treatment is the Dirac delta in expressions (35) and (61). Note that within the RMF approximation, the Dirac delta functions can be removed by applying the appropriate identity and correct integration limits (for details, cf. Ref. [24], and references therein), which we closely follow as detailed in Appendix B. It is important to emphasize that this is no longer possible at the RHF level, due to the explicit momentum dependence of the nucleon self-energies. Hence, we explicitly incorporate the Dirac delta function in our numerical integration and apply a root-finding procedure.

In the numerical calculations of Eqs. (35) and (61), we also evaluate the Dirac delta in the RMF approximation, where we note that within this approach, one can easily integrate out ϕ_{13} and ϕ_{24} to obtain $(2\pi)^2$. All integrals are evaluated using finite differencing based on the Gauss-Legendre quadrature. To find the angle root of the Dirac delta, we tested both a brute force approach and a globally convergent Newton-Raphson method, which yielded quantitatively comparable results. Only results that are in the range $-1 \leq \mu \leq 1$ are accepted; otherwise, the result is equal to zero⁵. The lower limit of the q_0 -integral is set to -400 MeV and the upper limit of the p_2 -integration is in the range of 1.0 – 1.5 GeV.

⁵ If the numerical iteration fails to converge within a finite number of steps, the delta is assumed to be zero.

A. Electronic charged-current processes

In the following, we evaluate the angle integrated neutrino absorption rate, $d\Gamma/dq_0$ (see Eq. (61)), for electron neutrino absorption on neutrons,

$$\nu_e + n \rightarrow e^- + p, \quad (62)$$

for the leading-order (LO) hadronic vertex (7) without form factors, see Eq. (8). This is shown in Fig. 3 for conditions A (top panels) and B (bottom panels), for selected incoming neutrino energies, E_1 (in log scale) from $\log(E_1/\text{MeV}) = 0.4$ – 2.0 . First, we validate our numerical procedure considering the vacuum differential absorption rates (left panels), i.e. all medium effects are set to zero and we apply the corresponding RHF neutron and proton chemical potentials. These results agree qualitatively with Ref. [24] (see their Fig. 2). Unfortunately, a quantitative comparison is not possible here due to the lack of certain data, e.g., neutron and proton chemical potentials.

Second, we evaluate the rates at the RMF level, shown in the right panels of Fig. 3. Therefore, we select TMA as a representative RMF parameterization (solid lines). For the further validation of the rate expressions at the RHF level, we distinguish the full approach, implementing the momentum-dependent medium modifications (dashed-dotted lines) and the semi-reduction of the RHF approach to TMA, by choosing constant TMA values for the neutron and proton scalar and time-like components of the self-energies (dotted lines) as well as zero vector self-energies, denoted as RHF(TMA). The values of the neutron and proton chemical potentials as well as non-zero self-energies, are listed in Table II. The results of the angle integrated neutrino absorption rates agree quantitatively with those of the actual RMF treatment

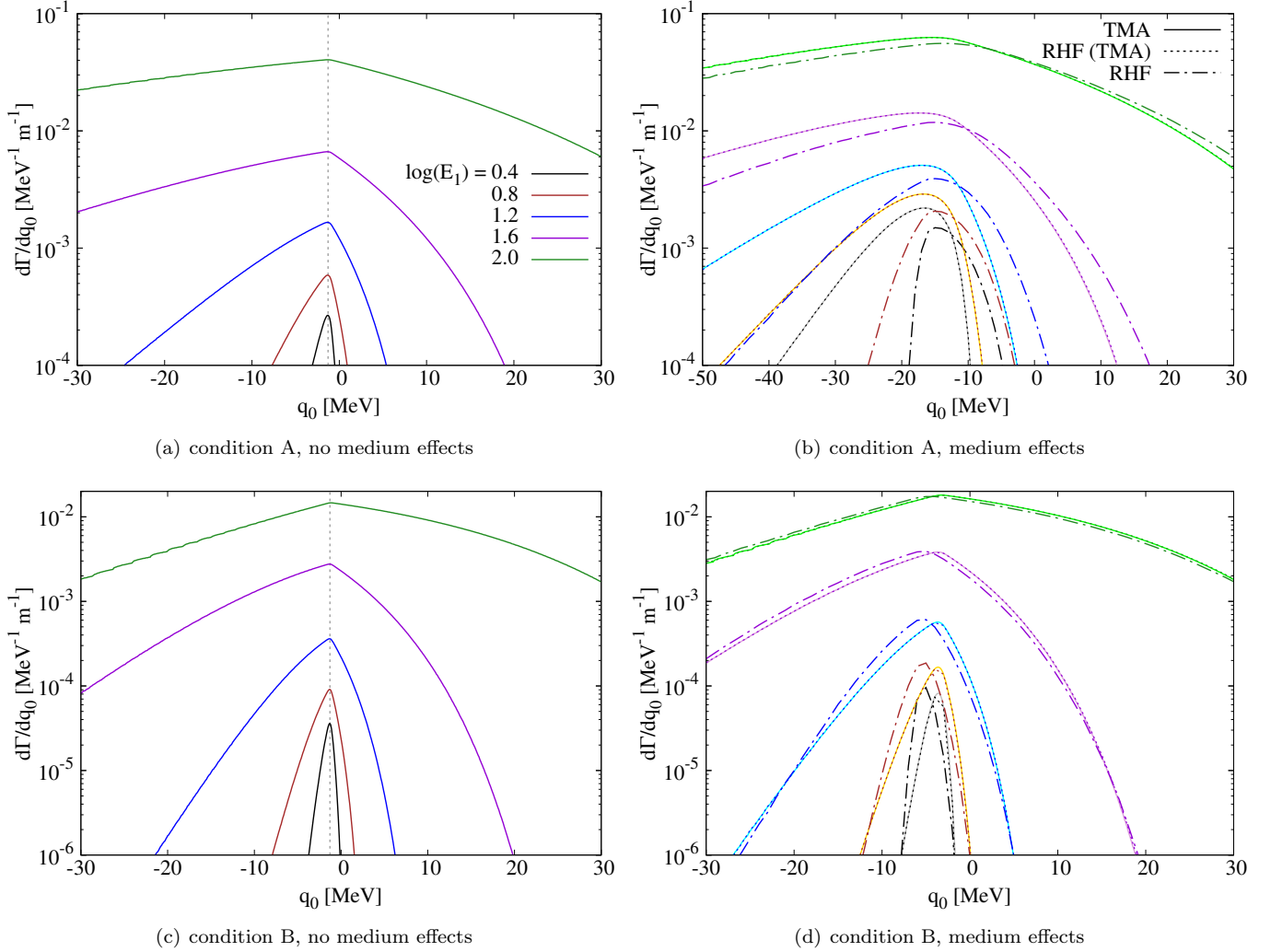


FIG. 3. Angle integrated neutrino absorption rate, $d\Gamma/dq_0$, for the process $\nu_e + n \rightarrow e^- + p$, as a function of energy transfer q_0 , for a selection of incoming neutrino energies E_1 (in log scale), for $\log(E_1/\text{MeV}) = 0.4-2.0$, for the two conditions A (top panels) and B (bottom panels), given in Tables I and II, for the leading-order (LO) hadronic vertex (7), Eq. (8). Results are shown for the vacuum rates (left panels), with zero nucleon self-energies, and with the medium effects included (right panels), where we distinguish the RMF approach (we select TMA as representative RMF model here), denoted as TMA (solid lines) and two RHF treatments. The latter employ the full momentum-dependent self-energies RMF (dashed-dotted lines) and the reduction to TMA, RHF(TMA), by choosing constant scalar and time-like component of the self-energies as well as zero vector self-energies (see text for details).

at all energies E_1 (see the dotted lines, which lie exactly on top of solid lines). This confirms the correct RMF limit of the corresponding numerical implementation of the momentum-dependent RHF model.

Third, moving to the comparison of RMF—again at the example of TMA—and RHF treatments, shown in Fig. 3 (solid and dashed-dotted lines), under the same conditions, it becomes evident that both exhibit qualitatively different q_0 dependencies, especially at low neutrino energies. We note here that, if no medium effects are considered, the rates peak at $q_0 = m_p - m_n = -1.293$ MeV, i.e. neutron-proton rest mass difference (gray, dashed vertical lines in the left panels of Fig. 3).

The peaks of the angle integrated neutrino absorption rates shift to larger negative values, if the medium modifications are taken into account at the RMF level, which is associated with the presence of non-zero self-energies (right panels)—the magnitude of the rate’s shifts at the RMF level is given by the effective (medium) Q -value [10, 16], $Q^* = m_p^* - m_n^* + (\Sigma_p^0 - \Sigma_n^0)$ (apply Eq. (30c) for the difference in the single-particle energies, $E_p - E_n$ at $\mathbf{p} = 0$), with neutron and proton effective masses and time-like self-energies, $m_{n/p}^*$ and $\Sigma_{n/p}^0$, respectively, which is generally negative under neutron-rich conditions. Therefore, especially at low neutrino energies, the peaks of the rates are located at Q^* , which

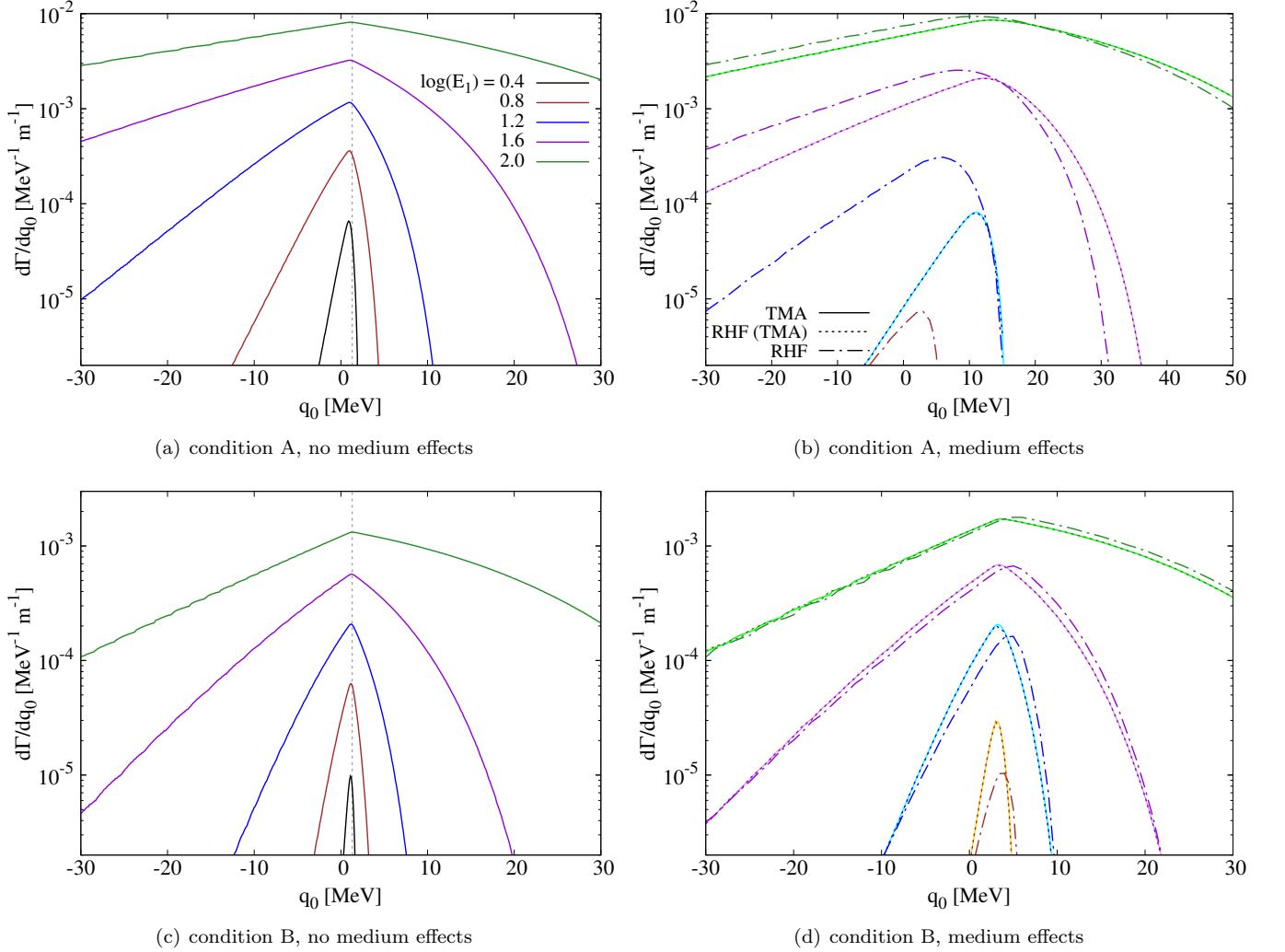


FIG. 4. The same as Fig. 3 but for the charged-current process involving electron antineutrinos, $\bar{\nu}_e + p \rightarrow e^+ + n$.

for TMA has values of $Q^* \approx -16$ MeV for condition A and $Q^* \approx -3.6$ MeV for condition B. We note further that for all RMF models under investigation here, we have $m_p^* - m_n^* = m_p - m_n$, since both neutron and proton have identical scalar self-energies (see the RMF rate expressions in Appendix B).

Fourth, investigating the rates within the RHF approach (dashed-dotted lines), we observe a shift of the rate's peaks back, towards less negative values of q_0 at higher densities (condition A) and more negative values of q_0 at lower densities (condition B), in comparison to TMA (solid lines). This finding is confirmed by calculating the modified Q^* -value within RHF, i.e. $Q^* = m_p - m_n + [\Sigma_p^S(0) - \Sigma_n^S(0)] + [\Sigma_p^0(0) - \Sigma_n^0(0)]$, assuming here constant values of the self-energies at the zero momentum and neglecting the generally small vector parts of the self-energies (middle panels in Fig. 2), i.e. $\Sigma_{n/p}^V = 0$ here. For condition A, we obtain $Q^* \approx -14.5$ MeV and for condition B, $Q^* \approx -5.4$ MeV. The differences of the rates between RHF and TMA treatments, shown in Fig. 3, are

attributed to the fact that neutron and proton feature naturally different scalar self-energies within the RHF approach (see expression (A6) in Appendix A), even without the explicit inclusion of the isovector-scalar δ -meson. This shift in the q_0 -dependence of the angle integrated neutrino absorption rates has important consequences for the energy-dependence of the neutrino opacity. We will return to this aspect later.

In the following, we repeat the calculations for electron antineutrino absorption on protons,

$$\bar{\nu}_e + p \rightarrow e^+ + n, \quad (63)$$

also here at the level of the leading-order hadronic vertex function without form factors. This can be done straightforwardly, with the proper replacements in expressions (35) and (61), i.e., replacing electron with positron, swapping neutron and proton propagators, and changing signs in several places in the lepton tensor components, as is detailed in Sec. III. The results are shown in Fig. 4, for the same conditions A (top panels) and

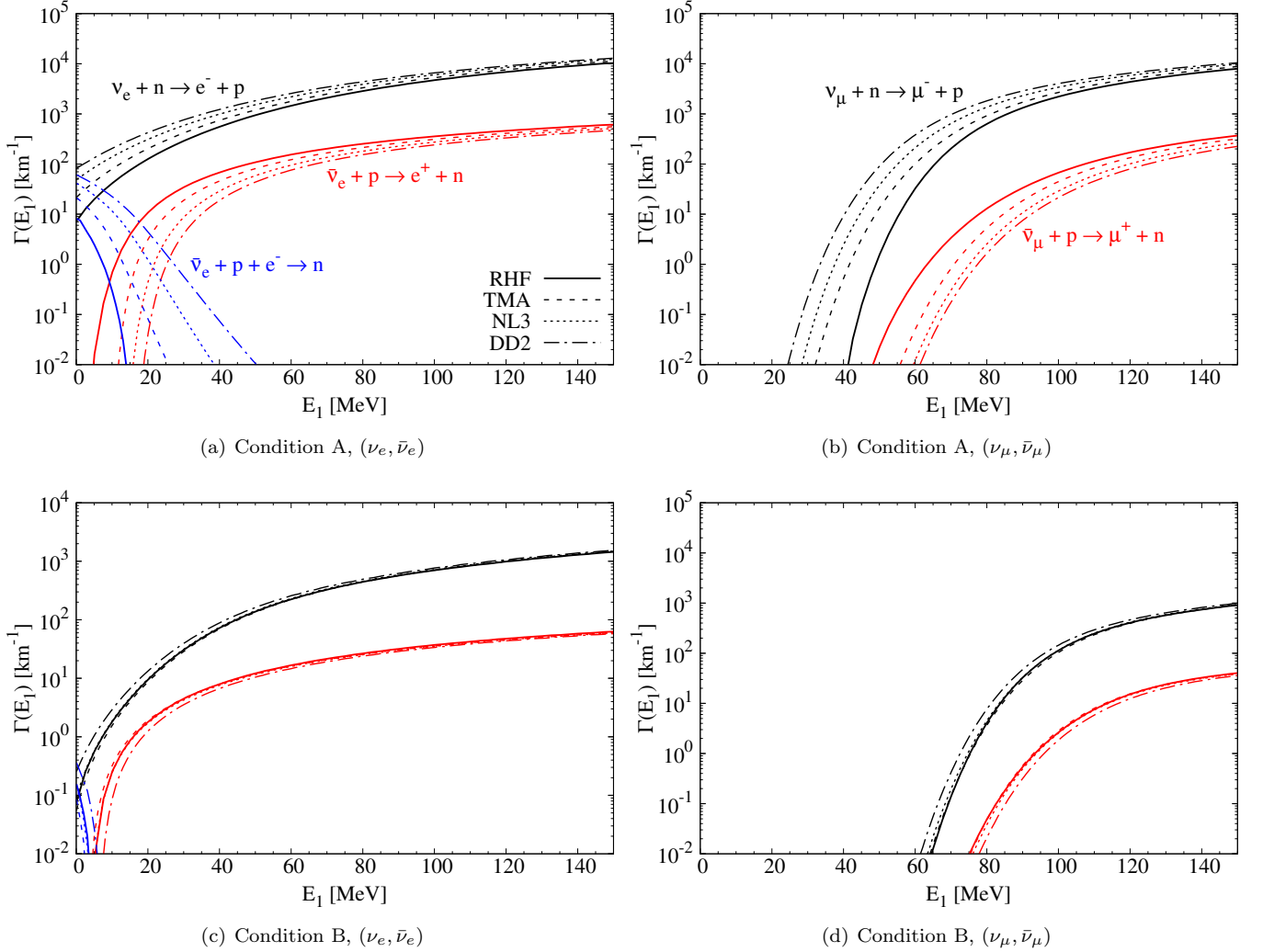


FIG. 5. Neutrino opacity as a function of the incoming (anti)neutrino energy, E_1 , for conditions A (top panels) and B (bottom panels), see Tables I and II, comparing RHF (solid lines), and our selection of representative RMF models: TMA (dashed lines), NL3 (dotted lines) and DD2 (dashed-dotted lines), employing here the full hadronic vertex (7), i.e. weak magnetism, pseudoscalar terms and form factors; see expressions (8)–(11). Black lines correspond to reactions involving neutrinos, red lines those for antineutrinos and blue lines for the inverse neutron decay, where we distinguish electronic charged-current processes (left panels) and muonic charged-current processes (right panels).

B (bottom panels) and for the same selection of incoming electron antineutrino energies, E_1 . Equivalently to Fig. 3, the left panels evaluate the rates without medium modifications, from which it becomes evident that the rates peak at $q_0 = m_n - m_p = 1.2935$ MeV (gray, dashed vertical lines in the left panels of Fig. 4), exactly as for the ν_e rates but with opposite sign. The reason therefore is well known, while for ν_e the conversion of neutrons to protons is exoenergetic, the reverse conversion of protons into neutrons is endoenergetic, in particular under neutron rich conditions. This has long been explored at the level of the zero-momentum transfer approximation [41] and at the RMF level [9].

As a consequence, in the case of medium-modified rates (right panels in Fig. 4), opposite to the behavior for ν_e

(see Fig. 3), the peaks of the rates are shifted towards larger positive values of q_0 at higher densities (condition A) and lower positive values of q_0 at lower densities (condition B). However, at the RMF and RHF level, these shifts are directly proportional to the corresponding medium Q -values, $Q^* = m_n^* - m_p^* + (\Sigma_n^0 - \Sigma_p^0)$ and $Q^* = m_n - m_p + [\Sigma_n^S(0) - \Sigma_p^S(0)] + [\Sigma_n^0(0) - \Sigma_p^0(0)]$, respectively, only at low densities (condition B) with the values given above for Q^* for ν_e with the extra minus sign, i.e. $Q_{\bar{\nu}_e}^* = -Q_{\nu_e}^*$, while at higher density (condition A), Q^* -values for ν_e and $\bar{\nu}_e$ do not give the same values with opposite sign. The reason for this is such that the expression for the antineutrino opacity is not entirely symmetric to the one for neutrino opacity both at the RMF and RHF level. Moreover, the behavior of the

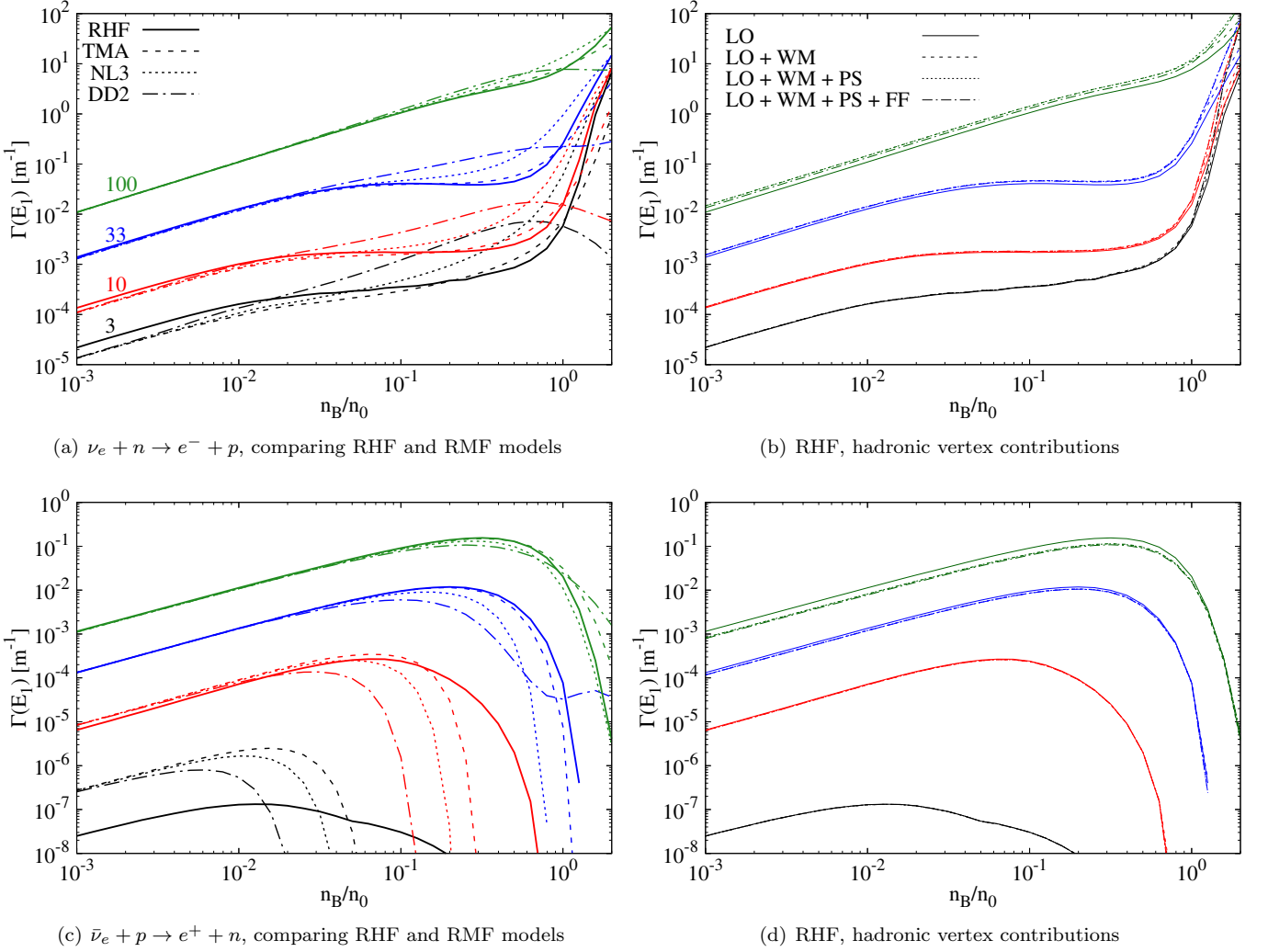


FIG. 6. Neutrino opacity as a function of the normalized baryon density, n_B , in units of the saturation density, n_0 , for a selection of (anti)neutrino energies of $E_1 = 3, 10, 33, 100$ MeV, corresponding to condition B (Tables I and II), for ν_e (top panels) and $\bar{\nu}_e$ (bottom panels). *Left panel:* Comparing our selection of representative RMF models: TMA (dashed lines), NL3 (dotted lines) and DD2 (dashed-dotted lines) and RHF approach (solid lines) at the leading-order hadronic vertex. *Right panel:* Rates at the RHF level comparing different contributions of the hadronic vertex (7), namely leading order (LO), weak magnetism (WM), pseudoscalar terms (PS) and form factors (FF).

magnitudes of RHF in comparison to TMA is opposite to those of ν_e in which they are suppressed (enhanced) for condition A (B), whereas the rates for $\bar{\nu}_e$ are enhanced (suppressed) for condition A (B). And finally, since the treatment of antineutrinos is not exactly symmetric to the one for neutrinos within RMF and RHF, we observe that we have a much stronger suppression of the $\bar{\nu}_e$ rate magnitudes at lower E_1 , especially for condition A and within RHF approach.

In order to further highlight the impact of the RHF treatment, in comparison to the RMF approach, we now turn to the discussion of the neutrino opacity (61), i.e. $\Gamma(E_1) = 1/\lambda_1$, for which we integrate the angle integrated electron neutrino absorption rate, $d\Gamma/dq_0$, over q_0 . Further below, we will return to the discussion of the

impact of the different contributions of the hadronic vertex (7), such as weak magnetism, pseudoscalar contributions, and form factors. Here, we employ the full vertex for the discussion of the opacity for both RMF and RHF approaches. Fig. 5 shows the opacity as a function of the incoming neutrino energy E_1 , comparing the RHF (solid line) and our selected RMF models: TMA (dashed lines), NL3 (dotted lines) and DD2 (dashed-dotted lines), for the two conditions A (top panels) and B (bottom panels). The left panels evaluate the electronic charged-current rates for ν_e (black lines) and $\bar{\nu}_e$, distinguishing between absorption (red lines) and inverse neutron decay (blue lines), and the right panels evaluate the muonic charged-current rates for ν_μ (black lines) and $\bar{\nu}_\mu$ (red lines).

To calculate neutrino opacity, Eq. (61), for the inverse

neutron decay (blue lines)

$$\bar{\nu}_e + p + e^- \rightarrow n, \quad (64)$$

the following modifications have to be introduced [14]:

- 1) the expressions of the lepton and hadron tensors are identical to the ones for the antineutrinos as introduced in Sec. III;
- 2) replacement of the lepton Pauli blocking, $1 - f_3(E_3) \rightarrow f_3(E_3)$;
- 3) the energy transfer of leptons becomes $q_0 = E_1 - E_3 \rightarrow E_1 + E_3$;
- 4) replacement in Eq. (B8), $E_3 \rightarrow -E_3$;
- 5) the integration limits of q_0 are from $E_1 + m_3$ to ∞ ;
- 6) since the process considered is described by Fig. 1 but with an arrow for p_3 in the opposite direction, which implies the usage of $G_3^<(p_3)$, it introduces a global minus sign.

Since the integration over q_0 is limited from above by $E_1 - m_3$ (only for ν_e and $\bar{\nu}_e$ absorptions), the most relevant for the behavior of $\Gamma(E_1)$ is the dependence of $d\Gamma/dq_0$ below this limit. For ν_e and $\bar{\nu}_e$ it covers all the peaks in both approximations. The neutrino opacities within the RHF are suppressed for ν_e and enhanced for $\bar{\nu}_e$, compared to the RMF rates, whereas DD2 exhibits the strongest enhancement of the ν_e opacity and the strongest suppression of the $\bar{\nu}_e$ opacity, respectively, due to the largest Σ^S and Σ^0 self-energies among all RMF models investigated here.

The magnitudes of enhancement and suppression depend on the conditions. At condition B (bottom panel), at lower density, the effect is smaller, which is associated with the shift of the effective Q -value—this can be identified through the drop in $\bar{\nu}_e$ opacity to zero—from $Q_{\text{TMA}}^* \approx 4$ MeV, $Q_{\text{NL3}}^* \approx 5$ MeV, $Q_{\text{DD2}}^* \approx 8$ MeV for the RMF models to $Q_{\text{RHF}}^* \approx 5$ MeV for RHF, compared to the higher baryon density at condition A (see Tables I and II), with Q -values ranging from $Q_{\text{TMA}}^* \approx 12$ MeV, $Q_{\text{NL3}}^* \approx 16$ MeV, $Q_{\text{DD2}}^* \approx 19$ MeV for RMF models to $Q_{\text{RHF}}^* \approx 5$ MeV for RHF.

Moreover, in the case of the inverse neutron decay (blue lines in the left panels of Fig. (5)), we observe a faster drop to zero of the opacity for condition B compared to condition A, with a much larger suppression within the RHF approximation, compared to the RMF approximations among which DD2 exhibits the largest enhancement due its large self-energies.

B. Muonic charged-current processes

The corresponding rates for the muonic charged-current reactions⁶,

$$\nu_\mu + n \rightarrow \mu^- + p, \quad \bar{\nu}_\mu + p \rightarrow \mu^+ + n, \quad (65)$$

are obtained by proper replacements of the electron with muon and positron with antimuon contributions in the rate expression (61), in particular by replacing the electron rest mass with that of muons, which has the biggest impact on the energetics in terms of modifying the effective Q -values, due to the large muon rest mass of $m_\mu = 105.658$ MeV [22] in comparison to the electron rest mass. The corresponding RMF opacities agree quantitatively with the data shown in Figs. 2 and 3 in Ref. [15] if we take the same underlying nuclear model. The comparison with the RHF rates shows the same suppression (enhancement) of the $\nu_\mu(\bar{\nu}_\mu)$ opacity as discussed above for the electronic charged-current reactions, but the shift of the effective Q -value between condition A and B is much stronger here in case of the RHF approach compared to the left panels in Fig. 5. Also, here, the magnitude depends on the conditions, ranging from $Q_{\text{TMA}}^* \approx 76$ MeV, $Q_{\text{NL3}}^* \approx 77$ MeV, $Q_{\text{DD2}}^* \approx 78$ MeV for RMF models to $Q_{\text{RHF}}^* \approx 75$ MeV for RHF at condition B and from $Q_{\text{TMA}}^* \approx 56$ MeV, $Q_{\text{NL3}}^* \approx 60$ MeV, $Q_{\text{DD2}}^* \approx 62$ MeV for RMF models to $Q_{\text{RHF}}^* \approx 48$ MeV for RHF at condition A.

C. Density dependence and contributions to the hadronic vertex

In the following, we will analyze the impact of the different contributions to the hadronic vertex (7), i.e. the leading order (LO) given by Eq. (8), and contributions from weak magnetism (WM), Eq. (9), pseudoscalar terms (PS), Eq. (10), and form factors (FF), Eq. (11). The resulting opacity for condition B is illustrated in Fig. 6 as a function of the baryon density for a selection of incoming neutrino energies of $E_1 = 3, 10, 33, 100$ MeV, for ν_e (top panels) and $\bar{\nu}_e$ (bottom panels).

To begin with, the left panels of Fig. 6 compare the opacity for the RMF and RHF models at the leading order of the hadronic vertex, confirming the previous analysis at the level of the neutrino energy-dependent opacity, i.e. the suppression (enhancement) of the $\nu_e(\bar{\nu}_e)$ opacity at low (anti)neutrino energies and intermediate densities. However, at supranuclear densities, we see that the RHF approach starts to dominate over all RMF models. We note here that above the saturation density, the uncertainty of the results within all the nuclear models starts to increase due to the lack of relevant experimental data.

⁶ There is no inverse neutron decay channel for muonic processes due to the large muon rest mass.

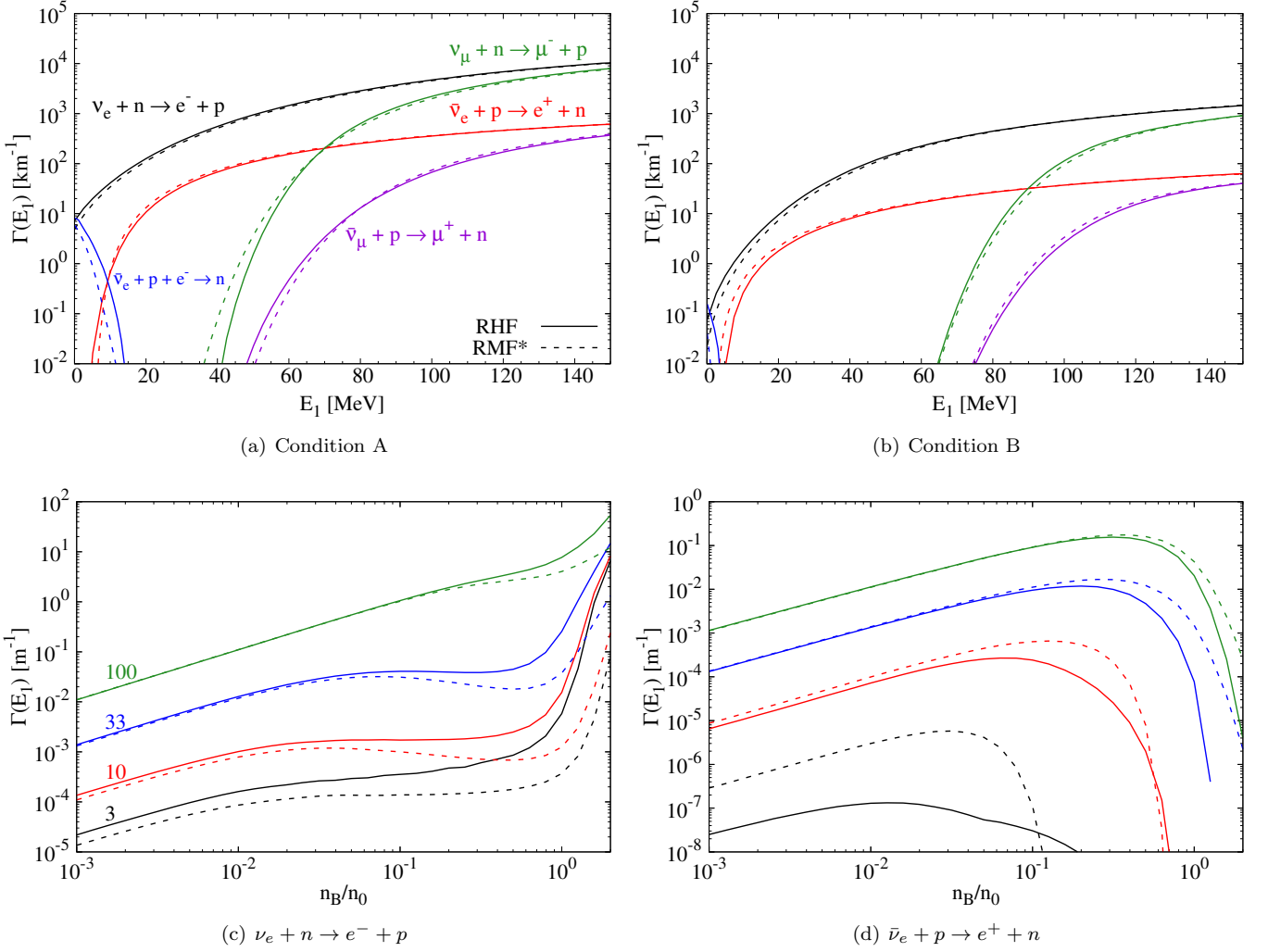


FIG. 7. Comparison of RHF (solid lines) and the reduced RMF* (dashed lines) models. *Upper panel:* Same as Fig. 5 for condition A in graphs (a) and (b) and condition B in graphs (c) and (d). *Lower panel:* Same as Fig. 6 for condition B.

From Fig. 6, we see that the different magnitudes of the neutrino opacity that appear with increasing density are attributed to the fact that the medium modifications due to the self-energies become increasingly larger with the lowest (largest) rates for RHF for ν_e ($\bar{\nu}_e$) at intermediate densities and the highest (lowest) rates for DD2 for ν_e ($\bar{\nu}_e$), for which we see that its magnitude starts to decrease for ν_e at supranuclear densities due to its density-dependent couplings, especially at smaller neutrino energies. Especially interesting is the modification of the effective medium modified Q -value for the $\bar{\nu}_e$, which systematically shifts towards higher densities, relevant especially for low and intermediate antineutrino energies.

We note here that the opacity for RMF and RHF approaches coincide towards low densities for high neutrino energies, for both ν_e and $\bar{\nu}_e$, which is due to the fact that the self-energies become negligible and the nuclear matter properties become indistinguishable. However, for low ν_e ($\bar{\nu}_e$) energies, there is a large mismatch between

RMF and RHF opacities. This is attributed to the difference between scalar self-energies in both models, present even at low baryon density, which we elaborate in detail in the Appendix C.

In the right panels of Fig. 6 we explore the different hadronic current contributions, expressions (8)–(11d), for varying density, but otherwise condition B (see Tables I and II). Compared to LO at densities below saturation density, especially at large neutrino energies, LO+WM+PS+FF increases ν_e rates, while both LO+WM and LO+WM+PS increase it even further by the same value, which confirms the findings of Ref. [15]. Concerning neutrino opacity for $\bar{\nu}_e$, we observe the largest decrease for LO+WM+PS+FF, while LO+WM and LO+WM+PS exhibit smaller but comparable decreases. Furthermore, the magnitude of the higher-order hadronic current contributions for ν_e increases with increasing density, in particular above saturation density, while for $\bar{\nu}_e$, the impact of those contri-

butions becomes negligible, due to medium suppression, for all neutrino energies.

V. NEUTRINO OPACITY FOR THE REDUCED RMF*

In order to analyze the large opacity differences observed between the RMF models and RHF, we develop another RMF parametrization as a specific reduction of the RHF model. Henceforth denoted as RMF*, it is based on the following mesons, (σ, ω, ρ) with standard meson-nucleon couplings. The resulting linear RMF model contains refitted σ and ω coupling constants in order to obtain the same nuclear saturation density and binding energy as for RHF (the saturation densities n_0 are given in the caption of Table II and more details are given in Sec. IV). In other words, the bulk nuclear matter properties of RHF and RMF* are nearly identical. The corresponding thermodynamic chemical potentials as well as self-energies are listed in Table II.

It becomes evident that, while the thermodynamic neutron and proton chemical potentials are of the same magnitude, for all nuclear models and both conditions A and B, RMF* has the smallest neutron-proton time-like self-energy difference. We obtain values for both neutrons and protons, also for the scalar self-energies, which correspond roughly to the mean RHF values (see Fig. 2). We note further that, as for the other RMF models, also for RMF*, we do not consider isospin splitting interactions due to δ -mesons, and hence neutron and proton scalar self-energies are identical.

The different self-energies of RMF* have important consequences for the kinematics of the neutrino opacity, shown in Fig. 7, comparing our RHF approach (solid lines) and RMF* (dashed lines). In the Figs. 7(a) and 7(b), we compare the opacity for conditions A and B, respectively, for different channels as a function of the incoming neutrino energy E_1 . It becomes evident that the RMF* results compare qualitatively with those of RHF, which we attribute to the similar nuclear matter properties. In particular, the medium modified Q^* -values and the associated thresholds for $\bar{\nu}_e$ are very close to those of the rates within the RHF treatment, $Q_{\text{RMF}^*}^* \approx \pm 6$ MeV for condition A and $Q_{\text{RMF}^*}^* \approx \pm 4$ MeV for condition B, distinguishing $\nu_e(-)$ and $\bar{\nu}_e(+)$. A similar trend is observed for the muonic charged-current reactions, especially for condition B. At increasing energy, on the order of $E_1 \simeq 40$ MeV, for the electronic charged-current reactions, and $E_1 \simeq 80$ MeV for the muonic reactions, the rates become identical for both conditions. It confirms that the deduced reduction agrees qualitatively with RHF approach. The differences become negligible towards lower densities. This density dependence is illustrated in Figs. 7(c) for ν_e and 7(d) for $\bar{\nu}_e$, for the same selection of incoming neutrino energies as before in Fig. 6, comparing our RHF approach (solid lines) and RMF* (dashed lines). We omit here muonic processes for

simplicity. Despite the qualitative match of the nuclear matter properties of RHF and RMF*, we observe a different behavior compared to other RMF models, in which RMF* with increasing density is more suppressed compared to RHF, which we attribute to the smallest value in $\Sigma_n^0 - \Sigma_p^0$ among all chosen RMF models. We emphasize here again the gap between both approaches at low (anti)neutrino energy and low baryon density, which is elaborated further in the Appendix C.

VI. SUMMARY AND CONCLUSIONS

In this article, we have performed novel calculations of the neutrino opacity for both electronic and muonic charged-current processes (1), with the inclusion of the inverse neutron decay, extending the previous calculations within the relativistic Hartree mean-field models [9, 15, 24] by incorporating momentum-dependent nucleon self-energies within the relativistic Hartree-Fock approach, including contributions from weak magnetism, pseudoscalar terms, and weak form factors. We derived the weak rate expressions from the neutrino self-energy within the RHF framework, for use in numerical calculations. We benchmarked the numerical results against the widely used RMF approach [15, 24].

The calculations show a consistent suppression of the neutrino opacity for ν_e and ν_μ within the RHF approach, compared to the RMF approximation, for both high and low temperatures and densities. For antineutrinos, $\bar{\nu}_e$ and $\bar{\nu}_\mu$, we observe the opposite tendency, i.e. an enhancement of the RHF opacity in comparison to the RMF results. The exceptions are the low neutrino energies with a generically large differences between RHF and RMF rates (see appendix C). We were able to attribute these large differences, comparing rates based on a selection of commonly employed RMF models and the RHF, to the presence of large neutron and proton scalar self-energy differences, which are naturally present within the RHF approach—we detail this in Appendix A—and otherwise negligible within RMF approximation. In addition, the momentum-dependence shows that this phenomenon is indeed non-negligible for a wide range of temperatures and densities. Concerning the inverse neutron decay, we see that it is largely suppressed within RHF compared to RMF. Furthermore, we perform a detailed analysis of different contributions of the hadron current, showing that they play a vital role especially at high (anti)neutrino energies.

This reduction of the rate differences between ν_e and $\bar{\nu}_e$, comparing the RHF treatment with the commonly employed RMF approach, due to the inclusion of neutron contributions to the proton scalar self-energy and vice versa within the RHF framework (see Appendix A), might have important consequences on the differences between ν_e and $\bar{\nu}_e$ fluxes and spectra in simulations of core-collapse supernovae, and in particular the long-term proto-neutron star deleptonization phase when the

neutrinospheres continuously shift to increasing densities [42]. We leave this important application of the here developed novel rates in simulations of core-collapse supernovae and binary neutron star mergers for future investigation.

ACKNOWLEDGMENTS

We wish to thank Gabriel Martínez-Pinedo for helpful discussions and for carefully reading the manuscript. This work was supported by the Polish National Science Center (NCN) under Grant Nos. 2023/49/B/ST9/03941 (K.S. and T.F.) and 2022/47/D/ST9/03092 (K.S.). The computations were performed at the Wrocław Center for Scientific Computing and Networking (WCSS).

DATA AVAILABILITY

The data that support the findings of this article are available from the authors based upon reasonable request.

Appendix A: Momentum-dependent self-energies within the RHF framework

The nuclear matter which is considered in the current paper in the calculations of the neutrino opacity is composed of two nucleons—protons (p) and neutrons (n)—described by the Dirac isodoublet $\psi = \begin{pmatrix} \psi_p \\ \psi_n \end{pmatrix}$, where the strong interaction is mediated by the exchange of the mesons [23]: two isoscalar-scalar σ and isoscalar-vector ω mesons, and two isovector-scalar π and isovector-vector ρ mesons. The Lagrangian can be decomposed as follows

$$\mathcal{L} = \mathcal{L}_0 + \mathcal{L}_I . \quad (\text{A1})$$

The free part is given by the following Lagrangian,

$$\begin{aligned} \mathcal{L}_0 = & \sum_{a=p,n} \bar{\psi}_a (i\gamma^\mu \partial_\mu - m_a) \psi_a + \frac{1}{2} (\partial_\mu \sigma \partial^\mu \sigma - m_\sigma^2 \sigma^2) \\ & - \frac{1}{4} \omega_{\mu\nu} \omega^{\mu\nu} + \frac{1}{2} m_\omega^2 \omega_\mu \omega^\mu + \frac{1}{2} (\partial_\mu \pi \cdot \partial^\mu \pi - m_\pi^2 \pi^2) \\ & - \frac{1}{4} \rho_{\mu\nu} \cdot \rho^{\mu\nu} + \frac{1}{2} m_\rho^2 \rho_\mu \cdot \rho^\mu , \end{aligned} \quad (\text{A2})$$

where the index $a = \{p, n\}$ refers to isospin and the field tensors are $\omega_{\mu\nu} = \partial_\mu \omega_\nu - \partial_\nu \omega_\mu$, and $\rho_{\mu\nu} = \partial_\mu \rho_\nu - \partial_\nu \rho_\mu$. The parameters in this model are the rest masses m_p , m_n , m_σ , m_ω , m_π , and m_ρ , of the fields ψ_p , ψ_n , σ , ω_μ , π^i , and ρ_μ^i , respectively. Note that there are three isovector mesons, i.e. $\pi^i = \{\pi^0, \pi^+, \pi^-\}$ and $\rho_\mu^i = \{\rho_\mu^0, \rho_\mu^+, \rho_\mu^-\}$.

The remaining interacting part of \mathcal{L} is given as follows,

$$\mathcal{L}_I = \bar{\psi} \left(-g_\sigma \sigma - g_\omega \gamma^\mu \omega_\mu - \frac{f_\pi}{m_\pi} \gamma_5 \gamma^\mu \partial_\mu \pi \cdot \boldsymbol{\tau} \right.$$

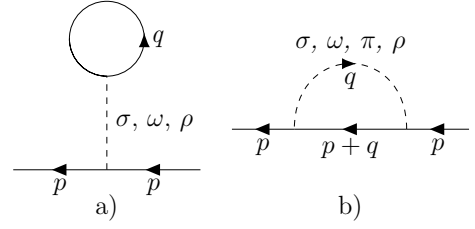


FIG. 8. Interacting Dirac Green's function at the second order, where a) is the Hartree (tadpole) diagram and b) is the Fock (exchange) diagram. Solid lines are described by the Dirac propagator and the dashed lines by the meson propagators.

$$-g_\rho \gamma^\mu \rho_\mu \cdot \boldsymbol{\tau} + \frac{f_\rho}{2m_n} \sigma_{\mu\nu} \partial^\nu \rho^\mu \cdot \boldsymbol{\tau} \Big) \psi , \quad (\text{A3})$$

where τ^i are the regular isospin Pauli matrices. In addition to the masses, here the parameters are the meson-nucleon coupling constants g_σ , g_ω , g_ρ , as well as f_π , f_ρ . The latter are the tensor coupling constants. We note here that there is an additional tensor coupling, f_ω , which is related to the isoscalar anomalous magnetic moment of the nucleon. However, it possesses a small value, compared to the other tensor couplings, and is therefore omitted in the present calculations [23]. For the pions, we choose the pseudovector (PV) representation. Despite the resulting Lagrangian being non-renormalizable, this choice avoids too strong πN interactions and nonphysical modifications of the nucleon spectrum at normal densities [43].

In terms of the Dirac Green's functions, the relativistic Hartree-Fock approximation is based on the two Feynman diagrams at the second order presented in Fig. 8 [19, 26, 27]. Due to the conservation of momentum at the vertices, the meson momentum is equal to zero in the Hartree diagram, Fig. 8(a), hence the π , the tensor ρ and the vector-tensor ρ terms in the interacting Lagrangian will not contribute. Moreover, when considering the mean-field approximation, both π^\pm and ρ^\pm mesons are not present as they would change the isospin, which is prohibited by charge conservation at the vertex. In the case of the Fock diagram, Fig. 8(b), all the mesons are involved. Additionally, in our considerations, we neglect the contribution of the retardation terms, i.e., $\propto E(p) - E(q)$, which describe the exchange of the nucleon energy between two vertices in the Fock diagram Fig. 8(b).

For both ρ and π mesons, we use the following decomposition of the inner products in the Lagrangian [44],

$$\boldsymbol{\tau} \cdot \boldsymbol{\pi} = \tau^3 \pi^0 + \sqrt{2} (\tau^+ \pi^+ + \tau^- \pi^-) , \quad (\text{A4})$$

$$\boldsymbol{\tau} \cdot \boldsymbol{\rho}_\mu = \tau^3 \rho_\mu^0 + \sqrt{2} (\tau^+ \rho_\mu^+ + \tau^- \rho_\mu^-) , \quad (\text{A5})$$

where $\tau^\pm = \frac{1}{2} (\tau^1 \pm i\tau^2)$ and $(\tau^i)^2 = (\tau^3)^2 + 2\tau^+ \tau^- + 2\tau^- \tau^+$. Note that for the charged mesons exchanged, an additional factor of $\sqrt{2}$ arises at a vertex. If no mixing

of the nucleons is considered, as in the case of symmetric nuclear matter, only the first term with τ^3 will contribute to the Feynman rules, with +1 for protons and -1 for neutrons.

The momentum-dependent nucleon self-energies are decomposed as in Eq. (29) [23] and their explicit forms for asymmetric nuclear matter [45] for non-zero temperature [46–48] are given as follows:

$$\begin{aligned} \Sigma_a^S(p) = & - \left(\frac{g_\sigma}{m_\sigma} \right)^2 n_S + \frac{1}{(4\pi)^2} \frac{1}{p} \left\{ \int_0^\infty dq q f_a(E_a) \left[\hat{M}_a(q) \sum_{i \in \mathcal{A}} B_{i,aa}(p, q) + \frac{1}{2} \hat{P}_a(q) D_{aa}(q, p) \right] \right. \\ & \left. + 2 \int_0^\infty dq q f_b(E_b) \left[\hat{M}_b(q) \sum_{j \in \mathcal{B}} B_{j,ab}(p, q) + \frac{1}{2} \hat{P}_b(q) D_{ab}(q, p) \right] \right\}, \end{aligned} \quad (\text{A6})$$

$$\begin{aligned} \Sigma_a^0(p) = & \left(\frac{g_\omega}{m_\omega} \right)^2 n_B \pm \left(\frac{g_\rho}{m_\rho} \right)^2 n_I + \frac{1}{(4\pi)^2} \frac{1}{p} \left\{ \int_0^\infty dq q f_a(E_a) \sum_{i \in \mathcal{A}} A_{i,aa}(p, q) \right. \\ & \left. + 2 \int_0^\infty dq q f_b(E_b) \sum_{j \in \mathcal{B}} A_{j,ab}(p, q) \right\}, \end{aligned} \quad (\text{A7})$$

$$\begin{aligned} \Sigma_a^V(p) = & \frac{1}{(4\pi)^2} \frac{1}{p} \left\{ \int_0^\infty dq q f_a(E_a) \left[\hat{P}_a(q) \sum_{i \in \mathcal{A}} C_{i,aa}(p, q) + \frac{1}{2} \hat{M}_a(q) D_{aa}(p, q) \right] \right. \\ & \left. + 2 \int_0^\infty dq q f_b(E_b) \left[\hat{P}_b(q) \sum_{j \in \mathcal{B}} C_{j,ab}(p, q) + \frac{1}{2} \hat{M}_b(q) D_{ab}(p, q) \right] \right\}, \end{aligned} \quad (\text{A8})$$

where $a = \{p, n\}$, $b = \{n \text{ if } a = p \text{ and } p \text{ if } a = n\}$ (which accounts for the nucleon mixing), $p = |\mathbf{p}|$, $q = |\mathbf{q}|$, + is for protons, - for neutrons, $f_{a/b}(E_{a/b})$ is the Fermi-Dirac distribution function with the expression given in the main text, where the single-particle energy $E_{a/b}$ is found via Eq. (30c), and we introduce the following sets: $\mathcal{A} = \{\sigma, \omega, \pi, \rho_V, \rho_T\}$ and $\mathcal{B} = \{\pi, \rho_V, \rho_T\}$, with the following notations:

$$\hat{P}_a(p) \equiv \frac{p_a^*(p)}{E_a^*(p)}, \quad (\text{A9})$$

$$\hat{M}_a(p) \equiv \frac{m_a^*(p)}{E_a^*(p)}, \quad (\text{A10})$$

and the baryon, scalar and isospin densities expressed as

$$n_B \equiv \sum_a \frac{1}{\pi^2} \int_0^\infty dq q^2 f_a(E_a) = n_p + n_n, \quad (\text{A11})$$

$$n_S \equiv \sum_a \frac{1}{\pi^2} \int_0^\infty dq q^2 f_a(E_a) \hat{M}_a(q), \quad (\text{A12})$$

$$n_I \equiv n_p - n_n. \quad (\text{A13})$$

All functions A , B and C are given explicitly in Table III with the following functions:

$$\theta_{i,ab}(p, q) \equiv \ln \left| \frac{\tilde{A}_{i,ab}(p, q) + 2pq}{\tilde{A}_{i,ab}(p, q) - 2pq} \right|, \quad (\text{A14})$$

$$\Phi_{i,ab}(p, q) \equiv \frac{\tilde{A}_{i,ab}(p, q)}{4pq} \theta_{i,ab}(p, q) - 1, \quad (\text{A15})$$

$$\tilde{A}_{i,ab}(p, q) \equiv p^2 + q^2 + m_i^2, \quad (\text{A16})$$

where $i = \{\sigma, \omega, \pi, \rho\}$.

The nucleon self-energies given by Eqs. (A6)–(A8) form a system of coupled non-linear equations which must be solved numerically. The method we implement here is based on the globally convergent Newton-Raphson root-finding method for the N-dimensional nonlinear system of equations. The coupled nucleon self-energies are solved for the given neutron and proton chemical potentials (μ_n and μ_p , respectively), where we start the numerical procedure at high density corresponding to high chemical potentials with the initial guesses, which are momentum-independent. Then, the obtained values of the self-energies are used to find the next values for a lower chemical potential, until we reach the required sub-nuclear density. In the implementation of the Newton-Raphson method, we create two 20-point momentum grids, $p_a \in \{p_1, \dots, p_{20}\}$ for $a = \{p, n\}$, using the 20-point Gauss-Legendre integration method, which we find to be sufficient, where $p_{20} = 5p_F$ is the maximum p taken as 5 times the Fermi momentum of the same infinite symmetric nuclear matter computed at zero temperature. Here, the proton or neutron chemical potential is compared to values of the chemical potential above the gas-liquid phase transition⁷ and the corresponding p_F is taken; oth-

⁷ At sub-saturation density, the presence of the gas-liquid phase transition at low temperatures features multiple solutions.

TABLE III. RHF functions, which appear in Eqs. (A6)–(A8), where $p = |\mathbf{p}|$, $q = |\mathbf{q}|$, and the other functions are defined in Eqs. (A14)–(A16), where all (p, q) and ab dependencies are omitted for clarity.

i	A_i	B_i	C_i
σ	$g_\sigma^2 \theta_\sigma$	$g_\sigma^2 \theta_\sigma$	$-2g_\sigma^2 \Phi_\sigma$
ω	$2g_\omega^2 \theta_\omega$	$-4g_\omega^2 \theta_\omega$	$-4g_\omega^2 \Phi_\omega$
π	$\left(\frac{f_\pi}{m_\pi}\right)^2 [-m_\pi^2 \theta_\pi + 4pq]$	$-\left(\frac{f_\pi}{m_\pi}\right)^2 [m_\pi^2 \theta_\pi - 4pq]$	$-2\left(\frac{f_\pi}{m_\pi}\right)^2 [pq\theta_\pi - (p^2 + q^2)\Phi_\pi]$
ρ_V	$2g_\rho^2 \theta_\rho$	$-4g_\rho^2 \theta_\rho$	$-4g_\rho^2 \Phi_\rho$
ρ_T	$\left(\frac{f_\rho}{2m_n}\right)^2 [-m_\rho^2 \theta_\rho + 4pq]$	$-3\left(\frac{f_\rho}{2m_n}\right)^2 [m_\rho^2 \theta_\rho - 4pq]$	$-4\left(\frac{f_\rho}{2m_n}\right)^2 [pq\theta_\rho - (p^2 + q^2 - m_\rho^2/2)\Phi_\rho]$
ρ_{VT}	$D = 12\frac{f_\rho g_\rho}{2m_n} [\theta_\rho p - 2\Phi_\rho q]$		

erwise, if the chemical potential is below the phase transition, we always take the same p_F at the phase transition. In total, there are 120 functions that form the system of equations to solve with 120 unknowns, i.e. 20 scalar self-energies, Σ_a^S , 20 time-like self-energies, Σ_a^0 , and 20 vector self-energies, Σ_a^V , each of which for protons and neutrons.

In the present paper, we choose parametrization e) of Ref. [23], however, with modified σ and ω coupling constants, in order to obtain a better nuclear binding energy at saturation density, $n_0 = 0.15 \text{ fm}^{-3}$, due to the missing $\pm 4pq$ terms in the functions A_π , A_{ρ_T} , B_π and B_{ρ_T} in Ref. [23] (see Table III). We employ the following model parameters for the rest masses: $m_n = 939.565 \text{ MeV}$, $m_p = 938.272 \text{ MeV}$, $m_\sigma = 440 \text{ MeV}$, $m_\omega = 783 \text{ MeV}$, $m_\rho = 770 \text{ MeV}$ and $m_\pi = 138 \text{ MeV}$, as well as the following coupling constants: $g_\sigma^2/4\pi = 5.33$, $g_\omega^2/4\pi = 10.01$, $g_\rho^2/4\pi = 0.55$, $f_\pi^2/4\pi = 0.08$ and $f_\rho/g_\rho = 3.7$.

Appendix B: Neutrino opacity within the RMF approximation

In this appendix, we revisit the essential formalism for the calculations of the neutrino absorption rate within the RMF approximation [19] and point out a number of differences in the final expressions compared to Ref. [24]. In this approach, the dressed nucleon quantities are those in Eqs. (30a)–(30c), except that the nucleon self-energies are momentum independent given as follows,

$$\Sigma_a^S = -\frac{g_\sigma^2}{m_\sigma^2} n_S, \quad (\text{B1})$$

$$\Sigma_a^0 = \frac{g_\omega^2}{m_\omega^2} n_B \pm \frac{g_\rho^2}{m_\rho^2} n_I, \quad (\text{B2})$$

where n_B , n_S and n_I are given by Eqs. (A11)–(A13), respectively, + is for protons, – for neutrons, and the vec-

tor part of the self-energy is $\Sigma_a^V = 0$, such that $p_a^* = p_a$, due to rotational invariance, which is assumed for nuclear matter. We note here that $\Sigma_n^S = \Sigma_p^S$, which is no longer true in the RHF approximation and in the DD2 model, all the meson-nucleon coupling constants are density dependent, which requires adding the rearrangement term, Σ_0^R , in the time-like self-energy (Eq. (B2)) as given in [30, 31].

In this formalism, the differential absorption rate can be obtained from Eq. (35) with the modified RMF effective quantities, which depend no longer on momentum but only on bulk properties of the nuclear medium, and the modified \tilde{q}^μ , as follows

$$\frac{d\Gamma(E_1)}{dE_3 d\mu_{13}} = \frac{G_F^2 C^2}{32\pi^2} \frac{p_3}{E_3} \frac{1 - f_3(E_3)}{1 - \exp\{-(q_0 + \Delta\mu)/T\}} L_{\mu\nu} \mathcal{I}^{\mu\nu}, \quad (\text{B3})$$

where $L_{\mu\nu}$ is defined by Eq. (46) and

$$\begin{aligned} \mathcal{I}^{\mu\nu} &= -2 \int \frac{d^3 p_2}{(2\pi)^3} \text{Im} \tilde{\Pi}^{\mu\nu}(q_0, q) \\ &= \int \frac{d^3 p_2}{(2\pi)^2} \frac{f_2 - f_4}{4E_2^* E_4^*} \Lambda^{\mu\nu} \delta(\tilde{q}_0 + E_2^* - E_4^*), \end{aligned} \quad (\text{B4})$$

which we introduce here to make a connection with the final expressions derived in the integral forms in Ref. [24], where $\text{Im} \tilde{\Pi}^{\mu\nu}$ and $\Lambda^{\mu\nu}$ are given by Eqs. (25) and (36), respectively, with the effective quantities taken from the RMF approximation. Here, we introduce the following effective 4-momentum transfer $\tilde{q}_\mu = (\tilde{q}_0, \mathbf{q})$ with $\tilde{q}_0 = q_0 + \Delta U$, where $\Delta U = \Sigma_2^0 - \Sigma_4^0$ is the difference of the neutron and proton RMF time-like self-energies.

Following Eq. (37), the contracted $L_{\mu\nu}$ and $\mathcal{I}^{\mu\nu}$ tensors in Eq. (B3) can be written in general as

$$L_{\mu\nu} \mathcal{I}^{\mu\nu} = \sum_{i \in \mathcal{A}} C_i [L_L I_L^i + L_Q I_Q^i - 2L_{M+} I_{M+}^i]$$

$$-2L_{M-}I_{M-}^i + 2L_{T+}I_{T+}^i + 2L_{T-}I_{T-}^i], \quad (\text{B5})$$

where \mathcal{A} and \mathcal{C}_i are given in (38). All components of the lepton tensor are given by Eq. (49), where within the mean-field approximation the 4-momentum contractions are modified as follows,

$$p_1 \cdot q = \frac{q_\mu^2 - m_3^2}{2}, \quad (\text{B6})$$

$$p_1 \cdot \tilde{q} = p_1 \cdot q + \Delta U E_1, \quad (\text{B7})$$

$$p_1 \cdot \tilde{n} = -\frac{q_\mu^2}{2q} \left[E_1 + E_3 - \Delta U + 2\Delta U E_1 \frac{q_0}{q_\mu^2} + (q_0 + \Delta U) \frac{m_3^2}{q_\mu^2} \right], \quad (\text{B8})$$

$$\tilde{n} \cdot q = -q\Delta U, \quad (\text{B9})$$

$$q \cdot \tilde{q} = q_\mu^2 + q_0\Delta U. \quad (\text{B10})$$

We note that, compared to [24], expression (B8) differs by a sign⁸.

Concerning $\mathcal{I}^{\mu\nu}$, for the sake of numerical calculations, it is useful to remove the Dirac delta in Eq. (B4), which we denote for now as $\delta(g(\mu))$, where $\mu \equiv \mu_{24}$. Then it can be rewritten as

$$\delta(g(\mu)) = \frac{\delta(\mu - \mu_0)}{|g'(\mu_0)|} \quad (\text{B11})$$

by applying the following property of the Dirac delta with μ_0 being the root of $g(\mu)$. In the RMF approach, we have the following definition,

$$\mu_0 = \frac{1}{2p_2q} [\tilde{q}_\mu^2\beta + 2E_2^*\tilde{q}_0], \quad (\text{B12})$$

where $\beta = 1 + (m_2^{*2} - m_4^{*2})/\tilde{q}_\mu^2$ and hence we obtain

$$\delta(\tilde{q}_0 + E_2^* - E_4^*) = \frac{\delta(\mu - \mu_0)}{p_2q} |E_2^* + \tilde{q}_0|. \quad (\text{B13})$$

To ensure that μ_0 is the correct root of $g(\mu)$, it must be in the range of $-1 \leq \mu_0 \leq 1$, which, after integrating over μ , imposes the new limit $\Theta(E_2^* - e_-)$ for E_2^* , where

$$e_- = -\beta \frac{\tilde{q}_0}{2} + \frac{q}{2} \sqrt{\beta^2 - \frac{4m_2^{*2}}{\tilde{q}_\mu^2}}. \quad (\text{B14})$$

Applying Eqs. (B11) and (B13), Eq. (B4) can be rewritten as

$$\mathcal{I}^{\mu\nu} = \frac{1}{(4\pi)^2} \int d\Omega_{24} \int_0^\infty dp_2 p_2^2 \frac{f_2 - f_4}{E_2^* E_4^*} \Lambda^{\mu\nu} \frac{\delta(\mu - \mu_0)}{|g'(\mu_0)|} \quad (\text{B15})$$

$$= \frac{1}{(4\pi)^2} \frac{1}{q} \int d\Omega_{24} \int_{m_2^*}^\infty dE_2^* \delta(\mu - \mu_0) \times \Lambda^{\mu\nu} \Theta(E_2^* - e_-) (f_2 - f_4). \quad (\text{B16})$$

If the function $g(\mu)$ has a complicated form, we apply Eq. (B15), which is the case for the RHF approximation as detailed in Section III. In this case, the root μ_0 is obtained numerically, for which we employ Newton-Raphson method, being retained if $-1 \leq \mu_0 \leq 1$. Moreover, the derivative $g'(\mu_0)$ must also be evaluated numerically. Contrary, in the RMF approximation, we instead use Eq. (B16).

The decomposition of $\Lambda^{\mu\nu}$ in Eq. (B16) is given by Eqs. (51)–(58), however, the 4-momentum contractions must be replaced by the following expressions:

$$p_2^* \cdot \tilde{q} = E_2^* E_4^* - p_2 q \mu \xrightarrow{\mu=\mu_0} -\frac{1}{2} \beta \tilde{q}_\mu^2, \quad (\text{B17})$$

$$p_2^* \cdot \tilde{n} = E_2^* q - p_2 \tilde{q}_0 \mu \xrightarrow{\mu=\mu_0} -\frac{\tilde{q}_\mu^2}{2q} [2E_2^* + \tilde{q}_0 \beta], \quad (\text{B18})$$

where the arrow indicates the substitution of the angle root as given in Eq. (B12), which would be the case after imposing the Dirac delta in $\mathcal{I}^{\mu\nu}$, Eq. (B16).

Taking into account the form of \mathcal{I} given by Eq. (B16), we define the following integrals:

$$I_Q = \frac{\tilde{q}_\mu^2}{4\pi q} \int_{e_-}^\infty dE_2^* (f_2 - f_4), \quad (\text{B19})$$

$$I_L = -\frac{\tilde{q}_\mu^2}{4\pi q^3} \int_{e_-}^\infty dE_2^* (f_2 - f_4) [2E_2^* + \tilde{q}_0 \beta]^2, \quad (\text{B20})$$

$$I_M = -\frac{\tilde{q}_\mu^2}{4\pi q^2} \int_{e_-}^\infty dE_2^* (f_2 - f_4) [2E_2^* + \tilde{q}_0 \beta], \quad (\text{B21})$$

$$I_T = -\frac{1}{2} I_L + \left(\frac{2m_2^{*2}}{\tilde{q}_\mu^2} - \frac{\beta^2}{2} \right) I_Q. \quad (\text{B22})$$

Based on these definitions, and applying Eqs. (B17)–(B18), along with imposing $\delta(\mu - \mu_0)$, the non-zero tensor components of Eq. (B4) can be cast into the following integral forms with the use of Eqs. (51)–(58):

1. Vector:

$$I_Q^V = (\lambda^2 + \sigma_- - 1) I_Q, \quad (\text{B23})$$

$$I_L^V = I_L + \sigma_- I_Q, \quad (\text{B24})$$

$$I_{T+}^V = I_T + \sigma_- I_Q, \quad (\text{B25})$$

$$I_{M+}^V = \lambda I_M, \quad (\text{B26})$$

where $\lambda = \beta - 1$ and $\sigma_\pm = 1 - (m_2^* \pm m_4^*)^2 / \tilde{q}_\mu^2$.

2. Axial-vector:

$$I_Q^A = (\lambda^2 + \sigma_+ - 1) I_Q, \quad (\text{B27})$$

⁸ We confirm $q_0 + \Delta U$ instead of $q_0 - \Delta U$ [24].

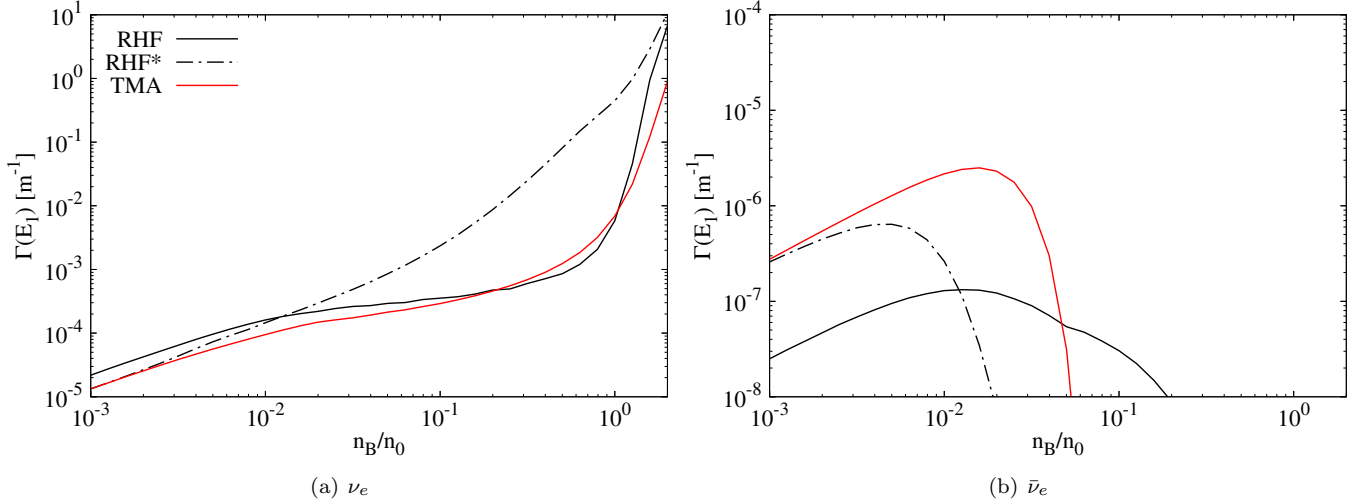


FIG. 9. Neutrino opacity, at the leading-order hadronic vertex contributions, as a function of the normalized number density, n_B , in units of the saturation density, n_0 , corresponding to condition B for neutrino (left panel) and antineutrino (right panel), at the incoming (anti)neutrino energy of $E_1 = 3$ MeV. The results are shown for the RHF and TMA rates (solid black and red lines, respectively). On top of that, we use a hybrid version of RHF approach denoted as RHF* (dashed-dotted line) in which we consider only one scalar self-energy for both neutrons and protons as explained in the main text.

$$I_L^A = I_L + \sigma_+ I_Q, \quad (\text{B28})$$

$$I_{T+}^A = I_T + \sigma_+ I_Q, \quad (\text{B29})$$

$$I_{M+}^A = \lambda I_M. \quad (\text{B30})$$

3. Tensor:

$$I_L^T = \frac{\tilde{q}_\mu^2}{4M_N^2} \left[\left(\sigma_- - \beta^2 + \frac{4m_2^{*2}}{\tilde{q}_\mu^2} \right) I_Q - I_L \right], \quad (\text{B31})$$

$$I_{T+}^T = \frac{\tilde{q}_\mu^2}{4M_N^2} \left[\left(\sigma_- - \beta^2 + \frac{4m_2^{*2}}{\tilde{q}_\mu^2} \right) I_Q - I_T \right], \quad (\text{B32})$$

with small differences arising, compared to Eqs. (57) and (58) in Ref. [24]⁹.

4. Pseudoscalar:

$$I_Q^P = -\frac{q_\mu^2}{M_N^2} I_Q. \quad (\text{B33})$$

5. Vector axial-vector:

$$I_{T-}^{VA} = -2i I_M. \quad (\text{B34})$$

6. Vector tensor:

$$I_L^{VT} = \left(2 \frac{m_2^*}{M_N} + \Delta\beta \right) I_Q, \quad (\text{B35})$$

$$I_{T+}^{VT} = \left(2 \frac{m_2^*}{M_N} + \Delta\beta \right) I_Q, \quad (\text{B36})$$

$$I_{M+}^{VT} = -\frac{\Delta}{2} I_M, \quad (\text{B37})$$

where Δ is given below Eq. (56c).

7. Axial-vector tensor:

$$I_{T-}^{AT} = -i \left(2 \frac{m_2^*}{M_N} + \Delta \right) I_M, \quad (\text{B38})$$

We note that also here for the vector tensor and axial-vector tensor terms, we find small differences compared to the literature¹⁰.

8. Axial-vector pseudoscalar:

$$I_Q^{AP} = -2 \left(\Delta\beta + 2 \frac{m_2^*}{M_N} \right) I_Q, \quad (\text{B39})$$

$$I_{M+}^{AP} = -\Delta I_M. \quad (\text{B40})$$

From the differential absorption rate, Eq. (B3), we can calculate the neutrino opacity by expressing it in terms of the integrals over q_0 and q , which are connected to E_3 via Eq. (59) and through μ_{13} via Eq. (60), respectively, (cf. Ref. [9]),

$$\Gamma(E_1) = \frac{G_F^2 C^2}{32\pi^2 E_1^2} \int_{-\infty}^{E_1 - m_3} dq_0 \int_{|E_1 - p_3|}^{E_1 + p_3} dq q$$

⁹ We find \tilde{q}_μ^2 instead of q_μ^2 , M_N^2 instead of m_2^2 in the denominator outside the brackets, and m_2^{*2} instead of m_2^2 in the numerator [24].

¹⁰ In the first terms in Eqs. (B35), (B36) and (B38), we obtain a factor of $2m_2^*/M_N$ instead of a factor of 2 as in Eqs. (59), (60) and (63) in Ref. [24].

TABLE IV. Neutron and proton self-energies for condition A and $l = e$ within the RHF ($\sigma, \omega, \rho, \pi$) with respect to 20 points of momentum p left-edged obtained from the Gauss-Legendre quadrature.

p	Σ^S	neutrons Σ^0	Σ^V	Σ^S	protons Σ^0	Σ^V
0.000	-185.511	163.564	-0.030	-152.035	116.903	-0.001
7.993	-185.507	163.555	-0.059	-152.032	116.902	-0.001
33.917	-185.451	163.448	-0.247	-151.983	116.894	-0.002
68.177	-185.286	163.134	-0.480	-151.840	116.870	0.012
118.970	-184.856	162.321	-0.764	-151.473	116.805	0.090
176.109	-184.113	160.950	-0.965	-150.857	116.687	0.288
247.252	-182.827	158.663	-1.006	-149.840	116.467	0.717
321.732	-181.091	155.744	-0.813	-148.552	116.145	1.354
406.804	-178.690	151.999	-0.366	-146.900	115.672	2.219
491.474	-175.953	148.102	0.208	-145.160	115.120	3.101
582.756	-172.740	143.962	0.859	-143.257	114.478	3.960
669.513	-169.565	140.259	1.432	-141.483	113.868	4.631
758.709	-166.303	136.784	1.936	-139.738	113.273	5.157
839.255	-163.446	133.966	2.308	-138.258	112.780	5.499
918.261	-160.782	131.499	2.596	-136.908	112.341	5.729
984.878	-158.668	129.634	2.788	-135.854	112.006	5.855
1046.542	-156.830	128.071	2.927	-134.948	111.724	5.926
1092.810	-155.528	126.994	3.010	-134.310	111.529	5.954
1131.596	-154.488	126.150	3.067	-133.804	111.376	5.965
1152.994	-153.933	125.706	3.094	-133.535	111.295	5.966

TABLE V. The same as in Table IV but for condition B.

p	Σ^S	neutrons Σ^0	Σ^V	Σ^S	protons Σ^0	Σ^V
0.000	-26.085	22.850	0.035	-21.896	14.583	0.006
7.993	-26.084	22.849	0.029	-21.895	14.583	0.012
33.917	-26.075	22.828	0.011	-21.881	14.588	0.052
68.177	-26.048	22.766	0.024	-21.841	14.602	0.108
118.970	-25.978	22.608	0.051	-21.743	14.633	0.200
176.109	-25.859	22.341	0.096	-21.591	14.673	0.318
247.252	-25.656	21.902	0.170	-21.364	14.712	0.480
321.732	-25.382	21.354	0.259	-21.108	14.727	0.651
406.804	-24.997	20.676	0.360	-20.811	14.713	0.825
491.474	-24.551	20.002	0.449	-20.520	14.676	0.964
582.756	-24.024	19.319	0.526	-20.217	14.625	1.074
669.513	-23.506	18.733	0.580	-19.945	14.575	1.143
758.709	-22.981	18.200	0.618	-19.685	14.526	1.184
839.255	-22.527	17.778	0.640	-19.471	14.485	1.202
918.261	-22.110	17.415	0.652	-19.279	14.449	1.205
984.878	-21.782	17.143	0.656	-19.132	14.422	1.199
1046.542	-21.500	16.918	0.656	-19.008	14.399	1.189
1092.810	-21.302	16.763	0.654	-18.921	14.383	1.179
1131.596	-21.144	16.642	0.651	-18.853	14.371	1.169
1152.994	-21.061	16.579	0.650	-18.817	14.365	1.163

$$\times \frac{1 - f_3(E_3)}{1 - \exp\{-(q_0 + \Delta\mu)/T\}} L_{\mu\nu} \mathcal{I}^{\mu\nu}. \quad (\text{B41})$$

Appendix C: Behavior of the low-energy neutrino opacity at low density

In Fig. 9, we extend the analysis of the behavior of the neutrino opacity at both low baryon density and low

(anti)neutrino energies, as discussed previously in Sec. IV (cf. Fig. (6)). To demonstrate the previously reported mismatch at low density between the standard RMF (as a representative, we choose TMA) and RHF rates, we evaluate the opacity at (anti)neutrino energy of $E_1 = 3$ MeV. To this end, we develop a hybrid version of the standard RHF approach, in order to identify the origin of the mismatch between the RMF and RHF opacities. To do this, we perform an ad hoc reduction of the RHF

approach to a hybrid version denoted as RHF* in which the proton scalar self-energy is enforced to be equal to the neutron one, i.e. $\Sigma_p^S(p) = \Sigma_n^S(p)$, in case of neutrinos, and neutron scalar self-energy is equal to the proton one, i.e. $\Sigma_n^S(p) = \Sigma_p^S(p)$, in case of antineutrinos. In both cases, it means that we have only one scalar self-energy, either $\Sigma_n^S(p)$ for neutrinos or $\Sigma_p^S(p)$ for antineutrinos.

Within this construction (black dashed-dotted lines in Fig. 9), the correct low-density TMA limit (and in general the RMF limit) of the opacity is reproduced (red solid lines), with the expected differences towards higher densities due to the different treatment of the medium effects within the RHF and TMA rates. We also see that RHF* model with only one momentum-dependent scalar self-energy differs largely from the RHF one at larger densities, which implies that the two scalar self-energies leave a non-negligible impact in asymmetric matter at

high baryon densities.

Appendix D: Tables of the Hartree-Fock self-energies

Data tables for the momentum-dependent RHF self-energies are given in Table IV for condition A and in Table V for condition B, separated into scalar Σ^S , time-like Σ^0 and vector Σ^V self-energies. The momentum p grid employs a 20-point Gauss-Legendre quadrature for the numerical integration procedures, ranging from $p = 0$ to $p \approx 1.2$ GeV (left-edged values). Here, we distinguish between neutrons (left columns) and protons (right columns) due to the consideration of asymmetric nuclear matter.

-
- [1] K. Hirata, T. Kajita, M. Koshiba, M. Nakahata, and Y. Oyama, *Physical Review Letters* **58**, 1490 (1987).
- [2] R. M. Bionta, G. Blewitt, C. B. Bratton, D. Casper, and A. Ciocio, *Physical Review Letters* **58**, 1494 (1987).
- [3] C. B. Bratton, D. Casper, A. Ciocio, R. Claus, M. Crouch, S. T. Dye, S. Errede, W. Gajewski, M. Goldhaber, T. J. Haines, T. W. Jones, D. Kielczewska, W. R. Kropp, J. G. Learned, J. M. Losecco, J. Matthews, R. Miller, M. Mudan, L. R. Price, F. Reines, J. Schultz, S. Seidel, D. Sinclair, H. W. Sobel, J. L. Stone, L. Sulak, R. Svoboda, G. Thornton, and J. C. van der Velde, *Phys. Rev. D* **37**, 3361 (1988).
- [4] E. N. Alexeyev, L. N. Alexeyeva, I. V. Krivosheina, and V. I. Volchenko, *Physics Letters B* **205**, 209 (1988).
- [5] M. Aglietta, G. Badino, G. Bologna, C. Castagnoli, A. Castellina, V. L. Dadykin, W. Fulgione, P. Galeotti, F. F. Kalchukov, F. F. Khalchukov, V. B. Kortchaguin, V. B. Korchagin, P. V. Kortchaguin, P. V. Korchagin, A. S. Malguin, A. S. Mal'Gin, V. G. Ryassny, V. G. Ryassnyj, O. G. Ryazhskaya, O. Saavedra, V. P. Talochkin, G. Trinchero, S. Vernetto, G. T. Zatsepin, and V. F. Yakushev, *EPL (Europhysics Letters)* **3**, 1315 (1987).
- [6] H.-T. Janka, *Annual Review of Nuclear and Particle Science* **75**, 425 (2025), arXiv:2502.14836 [astro-ph.HE].
- [7] T. Fischer, G. Guo, K. Langanke, G. Martínez-Pinedo, Y.-Z. Qian, and M.-R. Wu, *Progress in Particle and Nuclear Physics* **137**, 104107 (2024), arXiv:2308.03962 [astro-ph.HE].
- [8] I. Tamborra, *Nature Reviews Physics* **7**, 285 (2025), arXiv:2412.09699 [astro-ph.HE].
- [9] S. Reddy, M. Prakash, and J. M. Lattimer, *Phys. Rev. D* **58**, 013009 (1998), arXiv:astro-ph/9710115 [astro-ph].
- [10] G. Martínez-Pinedo, T. Fischer, A. Lohs, and L. Huther, *Phys. Rev. Lett.* **109**, 251104 (2012), arXiv:1205.2793 [astro-ph.HE].
- [11] L. F. Roberts, S. Reddy, and G. Shen, *Phys. Rev. C* **86**, 065803 (2012), arXiv:1205.4066 [astro-ph.HE].
- [12] T. Fischer, S. C. Whitehouse, A. Mezzacappa, F. K. Thielemann, and M. Liebendörfer, *Astron. Astrophys.* **517**, A80 (2010), arXiv:0908.1871 [astro-ph.HE].
- [13] L. Hüdepohl, B. Müller, H. T. Janka, A. Marek, and G. G. Raffelt, *Phys. Rev. Lett.* **104**, 251101 (2010), arXiv:0912.0260 [astro-ph.SR].
- [14] T. Fischer, G. Guo, A. A. Dzhiyev, G. Martínez-Pinedo, M.-R. Wu, A. Lohs, and Y.-Z. Qian, *Phys. Rev. C* **101**, 025804 (2020), arXiv:1804.10890 [astro-ph.HE].
- [15] G. Guo, G. Martínez-Pinedo, A. Lohs, and T. Fischer, *Phys. Rev. D* **102**, 023037 (2020), arXiv:2006.12051 [hep-ph].
- [16] L. F. Roberts, G. Shen, V. Cirigliano, J. A. Pons, S. Reddy, and S. E. Woosley, *Phys. Rev. Lett.* **108**, 061103 (2012), arXiv:1112.0335 [astro-ph.HE].
- [17] A. Mirizzi, I. Tamborra, H.-T. Janka, N. Saviano, K. Scholberg, R. Bollig, L. Hüdepohl, and S. Chakraborty, *Nuovo Cimento Rivista Serie* **39**, 1 (2016), arXiv:1508.00785 [astro-ph.HE].
- [18] A. Rusakov, A. S. Burrows, T. Wang, and D. Vartanyan, *arXiv e-prints*, arXiv:2602.09025 (2026), arXiv:2602.09025 [astro-ph.HE].
- [19] B. D. Serot and J. D. Walecka, *The relativistic nuclear many-body problem*, edited by J. W. Negele and E. Vogt, *Adv. Nucl. Phys.*, Vol. 16 (Plenum Press, New York, 1986).
- [20] M. Le Bellac, *Thermal field theory* (Cambridge university press, 2000).
- [21] R. L. Kobes and G. W. Semenoff, *Nuclear Physics B* **272**, 329 (1986).
- [22] S. Navas, C. Amsler, T. Gutsche, C. Hanhart, J. J. Hernández-Rey, C. Lourenço, A. Masoni, M. Mikhasenko, R. E. Mitchell, C. Patrignani, C. Schwananda, S. Spanier, G. Venanzoni, C. Z. Yuan, K. Agashe, G. Aielli, B. C. Allanach, J. Alvarez-Muñiz, M. Antonelli, E. C. Aschenauer, D. M. Asner, K. Assamagan, H. Baer, S. Banerjee, R. M. Barnett, L. Baudis, C. W. Bauer, J. J. Beatty, J. Beringer, A. Bettini, O. Biebel, K. M. Black, E. Blucher, R. Bonventre, R. A. Briere, A. Buckley, V. D. Burkert, M. A. Bychkov, R. N. Cahn, Z. Cao, M. Carena, G. Casarosa, A. Ceccucci, A. Cerri, R. S. Chivukula, G. Cowan, K. Cranmer, V. Crede, O. Cremonesi, G. D'Ambrosio, T. Damour, D. de Florian, A. de Gouvêa, T. DeGrand,

- S. Demers, Z. Demiragli, B. A. Dobrescu, M. D’Onofrio, M. Doser, H. K. Dreiner, P. Eerola, U. Egede, S. Eidelman, A. X. El-Khadra, J. Ellis, S. C. Eno, J. Erler, V. V. Ezhela, A. Fava, W. Fetscher, B. D. Fields, A. Freitas, H. Gallagher, T. Gershon, Y. Gershtein, T. Gherghetta, M. C. Gonzalez-Garcia, M. Goodman, C. Grab, A. V. Griksan, C. Grojean, D. E. Groom, M. Grünewald, A. Gurtu, H. E. Haber, M. Hamel, S. Hashimoto, Y. Hayato, A. Hebecker, S. Heinemeyer, K. Hikasa, J. Hisano, A. Höcker, J. Holder, L. Hsu, J. Huston, T. Hyodo, A. Ianni, M. Kado, M. Karliner, U. F. Katz, M. Kenzie, V. A. Khoze, S. R. Klein, F. Krauss, M. Kreps, P. Križan, B. Krusche, Y. Kwon, O. Lahav, L. P. Lelouch, J. Lesgourgues, A. R. Liddle, Z. Ligeti, C. J. Lin, C. Lippmann, T. M. Liss, A. Lister, L. Littenberg, K. S. Lugovsky, S. B. Lugovsky, A. Lusiani, Y. Makida, F. Maltoni, A. V. Manohar, W. J. Marciano, J. Matthews, U. G. Meißner, I. A. Melzer-Pellmann, P. Mertsch, D. J. Miller, D. Milstead, K. Mönig, P. Molaro, F. Moortgat, M. Moskovic, N. Nagata, K. Nakamura, M. Narain, P. Nason, A. Nelles, M. Neubert, Y. Nir, H. B. O’Connell, C. A. J. O’Hare, K. A. Olive, J. A. Peacock, E. Pianori, A. Pich, A. Piepke, F. Pietropaolo, A. Pomarol, S. Pordes, S. Profumo, A. Quadt, K. Rabbertz, J. Rademacker, G. Raffelt, M. Ramsey-Musolf, P. Richardson, A. Ringwald, D. J. Robinson, S. Roesler, S. Rolli, A. Romaniouk, L. J. Rosenberg, J. L. Rosner, G. Rybka, M. G. Ryskin, R. A. Ryutin, B. Safdi, Y. Sakai, S. Sarkar, F. Sauli, O. Schneider, S. Schönert, K. Scholberg, A. J. Schwartz, J. Schwiening, D. Scott, F. Sefkow, U. Seljak, V. Sharma, S. R. Sharpe, V. Shiltsev, G. Signorelli, M. Silari, F. Simon, T. Sjöstrand, P. Skands, T. Skwarnicki, G. F. Smoot, A. Soffer, M. S. Sozzi, C. Spiering, A. Stahl, Y. Sumino, F. Takahashi, M. Tanabashi, J. Tanaka, M. Taševský, K. Terao, K. Terashi, J. Terning, U. Thoma, R. S. Thorne, L. Tiaator, M. Titov, D. R. Tovey, K. Trabelsi, P. Urquijo, G. Valencia, R. Van de Water, N. Varelas, L. Verde, I. Vivarelli, P. Vogel, W. Vogelsang, V. Vorobyev, S. P. Wakely, W. Walkowiak, C. W. Walter, D. Wands, D. H. Weinberg, E. J. Weinberg, N. Wermes, M. White, L. R. Wiencke, S. Willocq, C. L. Woody, R. L. Workman, W. M. Yao, M. Yokoyama, R. Yoshida, G. Zanderighi, G. P. Zeller, R. Y. Zhu, S. L. Zhu, F. Zimmermann, P. A. Zyla, J. Anderson, M. Kramer, P. Schaffner, W. Zheng, and Particle Data Group Collaboration, Phys. Rev. D **110**, 030001 (2024).
- [23] A. Bouyssy, J.-F. Mathiot, N. Van Giai, and S. Marcos, Phys. Rev. C **36**, 380 (1987).
- [24] L. F. Roberts and S. Reddy, Phys. Rev. C **95**, 045807 (2017), arXiv:1612.02764 [astro-ph.HE].
- [25] L. F. Roberts and S. Reddy, Phys. Rev. C **95**, 045807 (2017), arXiv:1612.02764 [astro-ph.HE].
- [26] S. Chin, Ann. Phys. **108**, 301 (1977).
- [27] C. Horowitz and B. D. Serot, Nucl. Phys. A **399**, 529 (1983).
- [28] H. Toki, D. Hirata, Y. Sugahara, K. Sumiyoshi, and I. Tanihata, Nucl. Phys. A **588**, c357 (1995), proceedings of the Fifth International Symposium on Physics of Unstable Nuclei.
- [29] G. A. Lalazissis, J. König, and P. Ring, Phys. Rev. C **55**, 540 (1997).
- [30] S. Typel and H. H. Wolter, Nucl. Phys. A **656**, 331 (1999).
- [31] A. Kumar, P. Thakur, and M. Sinha, Mon. Not. Roy. Astron. Soc. **530**, 501 (2024), arXiv:2404.01252 [astro-ph.HE].
- [32] M. Hempel and J. Schaffner-Bielich, Nucl. Phys. A **837**, 210 (2010), arXiv:0911.4073 [nucl-th].
- [33] T. Fischer, S. Typel, G. Röpke, N.-U. F. Bastian, and G. Martínez-Pinedo, Phys. Rev. C **102**, 055807 (2020), arXiv:2008.13608 [astro-ph.HE].
- [34] T. Fischer, M. Hempel, I. Sagert, Y. Suwa, and J. Schaffner-Bielich, European Physical Journal A **50**, 46 (2014), arXiv:1307.6190 [astro-ph.HE].
- [35] M. Hempel, T. Fischer, J. Schaffner-Bielich, and M. Liebendörfer, Astrophys. J. **748**, 70 (2012), arXiv:1108.0848 [astro-ph.HE].
- [36] A. W. Steiner, J. M. Lattimer, and E. F. Brown, Astrophys. J. **765**, L5 (2013), arXiv:1205.6871 [nucl-th].
- [37] T. Fischer, N.-U. Bastian, D. Blaschke, M. Cierniak, M. Hempel, T. Klähn, G. Martínez-Pinedo, W. G. Newton, G. Röpke, and S. Typel, Publ. Astron. Soc. Austr. **34**, e067 (2017), arXiv:1711.07411 [astro-ph.HE].
- [38] S. Kubis and M. Kutschera, Physics Letters B **399**, 191 (1997), arXiv:astro-ph/9703049 [astro-ph].
- [39] R. Bollig, H.-T. Janka, A. Lohs, G. Martínez-Pinedo, C. J. Horowitz, and T. Melson, Phys. Rev. Lett. **119**, 242702 (2017), arXiv:1706.04630 [astro-ph.HE].
- [40] J. M. Lattimer and F. Swesty, Nuclear Physics A **535**, 331 (1991).
- [41] S. W. Bruenn, Astrophys. J. Suppl. **58**, 771 (1985).
- [42] T. Fischer, G. Martínez-Pinedo, M. Hempel, and M. Liebendörfer, Phys. Rev. D **85**, 083003 (2012), arXiv:1112.3842 [astro-ph.HE].
- [43] T. Matsui and B. D. Serot, Ann. Phys. **144**, 107 (1982).
- [44] J. D. Bjorken and S. D. Drell, *Relativistic quantum mechanics*, edited by L. I. Schiff, International series in pure and applied physics (McGraw-Hill, New York, 1964).
- [45] B. Y. Sun, W. H. Long, J. Meng, and U. Lombardo, Phys. Rev. C **78**, 065805 (2008).
- [46] K. Soutome, M. Tomoyuki, and S. Koichi, Nucl. Phys. A **507**, 731 (1990).
- [47] S. Yang, B. N. Zhang, and B. Y. Sun, Phys. Rev. C **100**, 054314 (2019).
- [48] S. Yang, X. D. Sun, J. Geng, B. Y. Sun, and W. H. Long, Phys. Rev. C **103**, 014304 (2021).